11-17-2008

Short-Wave Infrared Diffuse Reflectance of Textile Materials

Terence Haran

SHORT-WAVE INFRARED DIFFUSE REFLECTANCE OF TEXTILE MATERIALS

by

TERENCE L. HARAN

Under the Direction of Dr. Nikolaus Dietz

ABSTRACT

This thesis analyzes the reflectance behavior of textiles in the short-wave infrared (SWIR) band (1 – 2 microns) in order to identify/design potential diagnostic tools that allow the remote detection of human presence in a scene. Analyzing the spectral response of fabrics in the SWIR band has gained significant interest in the remote sensing community since it provides a potential path to discriminate camouflaged clothing from backgrounds that appear similar to the object of interest in the visible band. Existing research, originating primarily from the textiles community, has thoroughly documented the behavior of clothing fabrics in the visible band. Other work has shown that the differences in spectral response in the SWIR band allows for discrimination of materials that otherwise have the same visible spectral response. This work expands on those efforts in order to quantify the reflectance behavior and to better understand the physical basis for that behavior.

INDEX WORDS: Diffuse reflectance, Textile materials, Short-wave infrared

SHORT-WAVE INFRARED DIFFUSE REFLECTANCE OF TEXTILE MATERIALS

by

TERENCE L. HARAN

A Thesis Submitted in Partial Fulfillment of the Requirements for the Degree of

Master of Science

in the College of Arts and Sciences

Georgia State University

2008

SHORT-WAVE INFRARED DIFFUSE REFLECTANCE OF TEXTILE MATERIALS

by

TERENCE L. HARAN

Committee Chair: Nikolaus Dietz

Committee: Unil Perera

Gisele Bennett

Electronic Version Approved:

Office of Graduate Studies
College of Arts and Sciences
Georgia State University
December 2008

ACKNOWLEDGEMENTS

TABLE OF CONTENTS

LIST OF FIGURES

LIST OF TABLES

1   Introduction

The short-wave infrared (SWIR) portion of the electromagnetic spectrum, defined in this application as wavelengths between 1.0 and 2.5 microns, represents an underutilized resource for optical imaging applications in low light conditions. This is due to a number of factors, most notably the historical lack of detector technology that was sufficiently sensitive to these wavelengths and also manufacturable at reasonable cost.   Recent advances in detector technology, particularly Indium Gallium Arsenide (InGaAs) materials that are producible in large pixel formats at affordable prices, have resulted in new interest in SWIR imaging.[1] This interest is compounded by several phenomenological advantages in this band, including the availability of more ambient illumination from the night sky as compared to other reflective imaging bands as well as the ability to distinguish concealed targets, such as people or vehicles, from the background. However, better understanding of the fundamental physics associated with SWIR phenomena, such as the reflectance of materials, is required to fully utilize these advantages. This chapter describes the motivation for employing SWIR sensors in low light imaging applications with an emphasis on the diffuse reflectance behavior of textile materials as a driving force behind that motivation.

Different parts of the scientific communities have developed their own definitions of the various optical wavebands over the years. The definitions used here are those that are generally accepted by the electro-optical imaging community and are generally divided based on the dominant phenomenology (reflective versus emissive), atmospheric transmission windows, and detector material sensitivity. In the region below 3 μm, target radiance is dominated solely by

reflected ambient illumination either from the sun, night sky, or man-made sources while in the region above that wavelength target radiance is dominated by emissive phenomenology in accordance with Planck's Blackbody Law. As a result, the reflective region below 3 μm is of primary interest for the purposes of this analysis. This region is subsequently subdivided into other regions based on human visual response and detector technology. The spectral response of the human eye is between 0.4 μm and 0.7 μm and therefore that region is known as the visible band. Silicon detectors, which represent the most common class of optical sensor, have a response from 0.2 μm to 1.0 μm, which leads to the definition of another band between 0.7 and 1.0 μm that is called the near infrared region. The portion of the reflective region above 1 μm is known as the short-wave infrared and extends to 2.5 μm. Between 2.5 μm and 3 μm the atmospheric transmission is very low and therefore no label has been assigned for that region since it is generally unsuitable for imaging applications. Table 1 shows the typical electro-optical spectral region designations along with the associated acronyms that are used throughout this thesis.

Table 1. Designations of Electro-Optical Spectral Regions

Spectral Region	Designation	Nominal Wavelengths (μm)
Ultraviolet	UV	0.2 – 0.4
Visible	Vis	0.4 – 0.7
Near-Infrared	NIR	0.7 – 1.0
Short Wave Infrared	SWIR	1.0 – 2.5
Mid Wave Infrared	MWIR	3.0 – 5.0
Long Wave Infrared	LWIR	8.0 – 12.0 (14.0)
Very Long Wave Infrared	VLWIR	> 20.0 ; < 100
Sub-MM Wave	SMM	> 100

Historically, the SWIR region has been relatively inaccessible for imaging applications due to the lack of large format high sensitivity detectors that responded to those wavelengths. Recent advances in detector technology have altered that condition and led to the current interest in SWIR phenomenology. These advances include the development of photocathode materials that exhibit sensitivity to SWIR radiation as well as large format focal plane arrays using Indium Gallium Arsenide (InGaAs) and Mercury Cadmium Telluride (HgCdTe) detector materials. Image Intensifiers that use photocathodes to convert incident light to an image useful for human interpretation are the technology of choice for low light imaging in the NIR band. Modern Generation 3 Image Intensifiers use GaAs as a photocathode, and such systems further involve the use of Cesium and/or Cs:O to activate the GaAs. The reason for the choice of Cesium is in part that it has the lowest work function of any element – increasing the efficiency of electron multiplication from a given source of light over previous photocathodes. Typical GaAs photocathodes cannot detect light in the SWIR range; however modifying the photocathode by altering the compound composition through bandgap engineering can extend the spectral response of photocathode and increase SWIR range sensitivity. This has been achieved in several devices that are targeted primarily at the range gated imaging market. [2]

The most significant advances in SWIR focal plane array technology have been produced using InGaAs as the detector material. These detectors are fabricated using InAs and GaAs alloys with the composition of each one tuned to achieve specific performance. Because the InGaAs layer is extremely thin, a substrate is required to support it. This creates a functional problem because the film and the substrate must be lattice matched. A common substrate layer for use with InGaAs is InP, however the need to lattice match the InGaAs to the substrate limits spectral response from 0.9 μm to 1.7 μm. Although that region covers the peak

of night sky illumination, it leaves a significant portion of the SWIR uncovered. Several groups have attempted to extend the spectral response to 2.5 μm using different techniques, including alternate substrates, bandgap engineering, and strained layers, with varying degrees of success. Despite this, the advances in InGaAs focal plane array technology that have enabled array formats up to 1280x1024 with high sensitivity at affordable cost have made this the technology of choice for SWIR applications. [3]

Mercury Cadmium Telluride is a very well known and flexible detector material for infrared applications that has been adapted for the SWIR region. It is the preferred material for infrared detectors because its cutoff wavelength can be controlled easily by varying the ratio of Cadmium to Mercury in the detector material. Furthermore, HgTe and CdTe have nearly identical lattice constants which allow its spectral response to be varied widely without the lattice mismatch problem that occurs with InGaAs detectors. The achievable detectivity in these materials can be quite high, especially when combined with cryogenic coolers to reduce dark noise. However, although HgCdTe detectors can be fabricated in large format arrays, the cost to do so is very high relative to other technologies. This has limited their utility in any application that requires large volume production.[4] More recent advances in avalanche photodiodes (APD) using HgCdTe provide an opportunity for a high gain SWIR detector at low bias voltages for a variety of applications, including active imaging using pulsed lasers. Cost challenges will still limit their utility barring a significant change in the fabrication process.[5-7]

A variety of other detectors are under development that could be applicable to the SWIR spectral region. Lead Salt detectors, specifically Lead Sulfide (PbS), are actually an old technology that has been resurrected based on recent advances in processing technology. These

results have shown the ability to fabricate sensitive arrays including an intrinsic gain mechanism which provides low light imaging performance.[8] Other researchers have focused on strained layer superlattice (SLS) structures that are comprised of multiple thin layers that have been designed to respond to incident radiation of particular wavelengths. These devices are potentially easy to fabricate using existing semiconductor processing infrastructure and have the potential for performance exceeding HgCdTe devices. However, SWIR SLS detector arrays have only recently been demonstrated in the laboratory so significantly more work is required before they can be used in other applications. All of these advances have combined to generate significant interest in the SWIR band for imaging applications, which in turn requires a better understanding of the phenomenology that drives performance in that region.[9]

Interest in the SWIR waveband is driven not only by the advances in detector technology described previously but also by potential phenomenological advantages in detecting objects using those detectors, particularly under low light conditions. As mentioned previously, target signatures in the SWIR waveband are dominated by reflection of external sources of illumination as opposed to thermal emission of radiation which occurs in the longer infrared wavelengths. The external illumination sources that contribute to reflected signatures are actually comprised of several components. The equation below provides a comprehensive summary of the processes impacting signatures in the reflection regime. [10]

$$L_{sensor}(\lambda) = \left[L_{lun}(\lambda, \vartheta_{lun}) + L_D(\lambda, atmos, \vartheta_{sky}) + \sum_{i=1}^{M} L_{obj}^i(\lambda, \alpha_i) \right] \cdot \rho_\lambda \cdot \tau_\lambda + L_{path}(\lambda) + L_{adj}(\lambda) \cdot \tau_\lambda$$

The equation can be used to compute the at-aperture spectral radiance onto a sensor, where:

L_{lun} = radiance directly incident on the object from the moon,

L_D = diffuse sky radiance,

L_{obj} = incident radiance due to reflections from other objects in the scene,

L_{path} = radiance from all sources scattered into the observation path,

L_{adj} = radiance scattered into the field of view by objects outside the field of view,

θ_{sky} = angular geometry between different sky areas and the object,

θ_{lun} = the angle between the moon and object,

ρ_λ = spectral reflectance of the object,

α_i = angle between the object and other objects in the scene, and

τ_λ = spectral transmission factor of the medium

The indirect, or diffuse, terms typically arise from either extended sources such as the sky or from radiation scattered from multiple diffuse surfaces. The term in the brackets represents the radiance incident on an object from multiple sources. The incident radiance will be reflected from the object in the direction of the sensor; ρ_λ represents the reflectance of the object. Propagation of this radiance through the atmosphere results in attenuation due to various processes, such as scattering and absorption; the transmission factor, τ_λ, provides a measure of the atmospheric transparency.

Another consequence of atmospheric propagation is provided by the second term in the equation. Designated as the path radiance, L_{path} represents the radiance from all sources that is scattered into the observation path between the object and the sensor. Both single and multiple scattering events will contribute to the overall path radiance. The last term in the equation, L_{adj}, represents the adjacency effect which is the scattering of radiance into the field of view by object areas outside the field of view of the sensor (or pixel).

All of these components have a geometric and environmental dependence. The explicit dependence of several of the terms on the exact viewing geometry includes θ_{lun}, the angle between the moon and object; θ_{sky}, the geometry between different sky areas and the object; and α_i, the angular relationship between the object and other objects in the scene. The dependence on the environmental state is implicit except for the *"atmos"* dependence given for the diffuse sky radiance term. The only terms explicitly left out are those arising from manmade sources. In this case, direct illumination from such sources would constitute another term similar to that of L_{lun}, the lunar illumination.

Examination of these equations reveals that two critical variables that determine the appearance of a particular object are its reflectance and the ambient illumination. For many applications, detection of humans is a critical requirement and the ability to do so is driven by the ambient illumination available for a particular application as well as the reflectance of common clothing materials. The presence of significant natural illumination at night in the SWIR band is the reason for much of the interest in that band for imaging applications. Diffuse night sky radiance arises from several terrestrial and extraterrestrial sources. Both manmade and natural sources contribute to the overall diffuse night sky radiance. Manmade sources originate from lighting employed in urban and rural areas and have been widely documented in literature from

7

the astronomical community on light pollution.[11-14] However, manmade light sources vary widely between locations and therefore are of less interest than natural sources for nighttime imaging. Natural sources of ambient illumination originate from several physical phenomena including airglow, zodiacal light, integrated starlight, diffuse galactic light, and extragalactic light. Each of these sources contributes to the various spectral regions at different radiance levels. Zodiacal light refers to sunlight reflected from interplanetary dust. Diffuse galactic light refers to starlight reflected from interstellar dust. Extragalactic light refers to the light contribution from unresolved, diffuse sources external to the Milky Way galaxy. There is also a scattering component that is the sum of the atmospheric scattering contribution from three diffuse sources: sky luminescence, zodiacal light, and galactic light.   Figure 1 shows the intensity levels for a variety of diffuse sky radiance sources as a function of wavelength. It is clear from this plot that there is significant night sky radiance in the SWIR region, primarily as a result of the night glow phenomenon.[15]
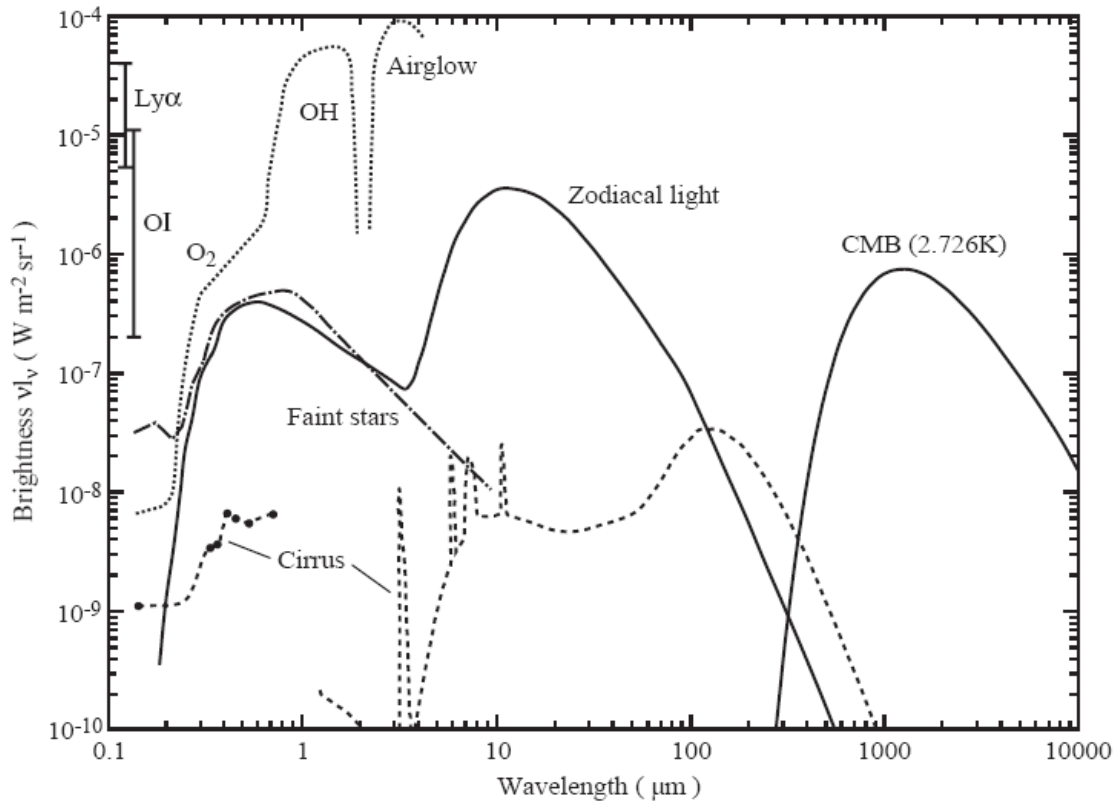
Figure 1. Intensity levels of typical diffuse sky radiance sources [15]

The nightglow phenomena originate from upper atmospheric layers located in the Mesosphere and lower Thermosphere regions (80–100 km in altitude). Early studies of this upper atmospheric region focused on characterizing the photochemical reactions and scattering mechanisms that produced ultraviolet radiation (day glow phenomena).[16] Subsequent investigations have expanded to include studies of the physical processes that produce visible and infrared radiation at night.[17] Fundamentally, nightglow results from chemical reactions in the upper atmosphere. During the day, photochemical reactions transform solar energy into chemical energy. O_2 disassociation at an altitude of 95 km and OH production at 87 km are the dominant reactions of importance for establishing reservoirs of energy for the visible and infrared spectral bands. At night, chemiluminescence, radiative recombination, and collisional

9

de-excitation become the predominant mechanisms for photon production.[18] In general, these reactions involve several chemical species and generate emissions spanning the far-ultraviolet to SWIR regions. Chemical reactions involving excited oxygen atoms and molecules result in the generation of photons at wavelengths between 0.68 and 1.0 μm with several emission lines below 0.68 μm. Reactions involving hydroxyl molecules (OH) generate radiation in the visible and infrared bands. Emissions from these latter reactions are the predominant source of background radiation in the 0.8–2.2 μm region. Though the radiation results from discrete emission lines, the OH lines are finely spaced, uniformly distributed, and relatively equal in strength over this spectral region. As a consequence, the radiation from the OH reactions has the appearance of a continuum.

The emission rate from the 0.8–2.2 μm region at night depends on several factors: solar flux, inclination of the ecliptic, and density of molecular oxygen. Solar flux has a dependence on the solar cycle that induces long term variability to the emission processes. Over the course of the annual orbit around the sun, the inclination of the ecliptic will change and create a seasonal variation for the incident solar flux. A geographic latitudinal dependence is also present. The inclination of the Earth creates a longer propagation path length for the incident solar flux as the latitude increases toward either pole. A longer path length results in larger attenuation of the incoming radiation. Collisional relaxation times add an additional time dependence, which translates to a longitudinal dependence. Figure 2 shows the major night sky radiance sources in the region below 2.5 microns.[3] The moon is modeled here as a poor reflector of the sun which is characterized in turn as a 5900K blackbody peaking at 490 nm. Tropospheric thermal radiation is represented by the 273K and 295K blackbody curves for cold and warm rights respectively. It is clear from these spectra that under full moon conditions the night sky radiance

is roughly equivalent between the SWIR and Visible/NIR regions as the slightly higher moon radiance in the VNIR region is negated by the wider spectrum in the SWIR region. However, under low or no moon conditions, there is significantly more (approximately an order of magnitude) radiance in the SWIR region as compared to the VNIR spectrum due to the enhanced airglow above 1 micron. Integrated starlight and zodiacal light are both fairly negligible even under no moon conditions and thermal radiation does not play a significant role except in extended SWIR applications that approach 2.5 microns.
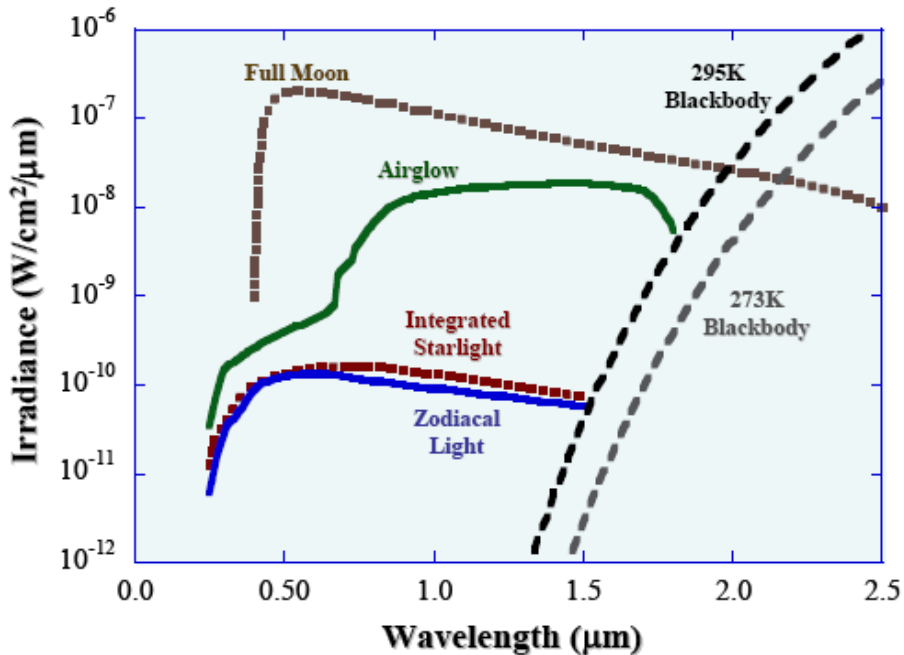
Figure 2. Dominant night sky illumination sources below 2.5 microns

In addition to the advantage in night sky illumination, there are other phenomenological benefits that favor the use of SWIR relative to other imaging bands. Compared to visible and NIR sensors, SWIR has better penetration through atmospheric obscurants, including smoke, dust, and fog, due to its longer wavelength. This is highly desirable since situations are frequently encountered where atmospheric conditions are less than ideal. Better anti-blooming

rejection make SWIR more desirable as well for scenes where bright objects (open flame for example) are mixed in with normal brightness objects. Detection of hidden targets is another potential advantage of SWIR since many man-made materials that have very different reflectance in the Visible/NIR have nearly identical reflectance in the SWIR band and that reflectance is typically very different from naturally occurring background materials.[19] Figure 3 shows an example of reflectance spectra below 2.5 microns for wood painted with black and green paint. Despite the disparate reflectances in the visible and NIR region, they are essentially identical above 1 micron and much higher than bare wood (represented by the bottom spectrum). This behavior has been observed for many different materials and is the basis of further study in this thesis. It is an important observation because it makes obscured targets much easier to detect, particularly when hidden in vegetation.[20] As an example, the images in Figure 4 were taken under starlight conditions and demonstrate the enhanced reflectance of clothing in the SWIR compared to the VNIR imagery.
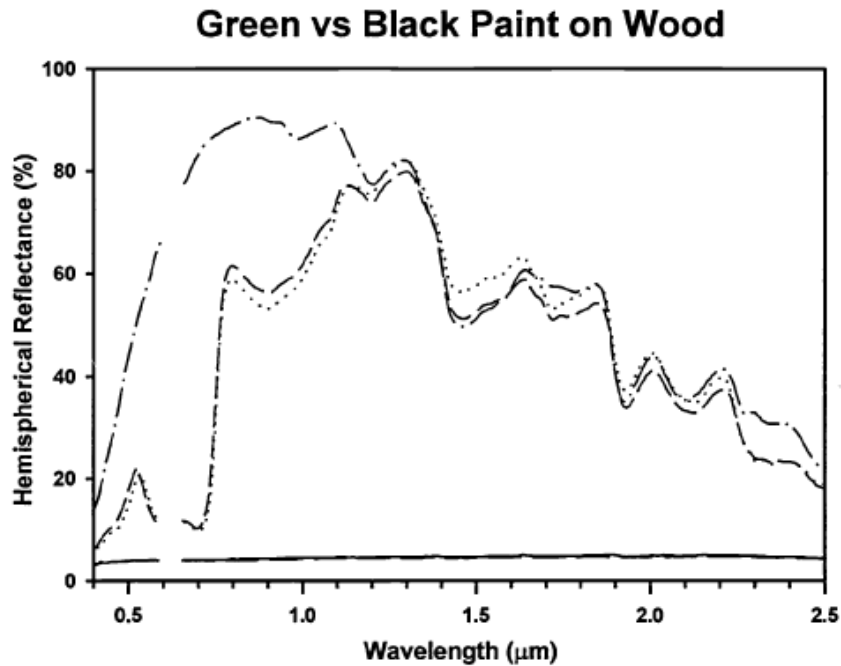
Figure 3. Reflectance spectra of black and green painted wood [20]

Figure 4. Night time VNIR and SWIR imagery [21]

2   Theories of Diffuse Reflectance

Incident light on a particular medium is affected by a number of different phenomena, including refraction, reflection, absorption, diffraction, and diffusion, while it propagates through the medium. The net effect on the behavior of the light varies widely depending on the properties of that particular medium; however some portion of the light will be reemitted with a spectrum of reflectance that is unique to that medium. Reflectance is defined here as the ratio of the reflected flux to the incident flux at a given wavelength and for a given measurement geometry. It is important to note that reflectance is a bidirectional property that is dependent on the source, material, and observer geometry and can only be fully characterized by the Bidirectional Reflectance Distribution Function (BRDF) that describes reflectance for all combinations of source and observer angles. These reflections are comprised of both a diffuse component, where reflections are scattered in all directions, and a specular component, where the light is reflected in accordance with Fresnel's law. A surface that displays ideal diffuse reflectance where light is scattered equally in all directions is described as Lambertian. Diffuse reflectance is of particular interest for understanding the appearance of materials, since most naturally occurring surfaces, including fabrics, are diffuse reflectors.

Reflectance is a critical property to describe targets in optical imaging applications at wavelengths below 3 microns where target radiance is dominated by the reflection of ambient illumination. In the visible band (defined as the 0.4 to 0.7 micron spectral region) the spectrum of the reflectance is particularly important since it uniquely describes the color of the object as perceived by human observers. As a result, a number of different models have been developed to predict reflectance in that portion of the spectrum. However, the reflectance of a medium is

equally important in other wavebands when using sensors that are sensitive to wavelengths outside of the visible band. A major objective of this thesis is to extend these existing models to the SWIR portion of the electromagnetic spectrum.

The basic interaction between light and the particles in a particular medium depends on the size of those particles relative to the wavelength of the light. Rayleigh scattering dominates for particles that are small compared to the wavelength, Fresnel reflection dominates when the particles and wavelength are of the same order, and Mie scattering dominates when the particles are much larger than the wavelength of the incident light. However, for intermediate cases such as those that commonly occur in textile materials, the scattering is more complex and cannot be handled with those theories. As a result, several widely employed theories have been developed that predict the diffuse spectral reflectance of different materials in the visible band. These theories all take different approaches to this problem based on the wave-particle duality that is inherent to light. For example, Mie employed an electromagnetic approach based on Maxwell's Equations [22] while Silvy used a particle driven technique that was based on photon flux density [23]. This chapter discusses the major theories that have been developed to predict spectral reflectance.

2.1 Kubelka and Munk Theory

Kubelka and Munk proposed a widely utilized theory in 1931 that uses a system of differential equations based on a simple model of a paint layer that is parallel to a plane support.[24] This theory expanded on Schuster's earlier theory to calculate the reflectance of a medium containing suspended particles.[25] The approach taken in the Kubelka-Munk theory utilized two fluxes passing through the material, one that is in the direction of incidence called i and one that is in the direction of reflectance called j. They also defined two physical constants,

k which represents absorption of the medium and *s* which represents scattering from the medium. These constants are the same independent of the thickness of the medium. Based on this setup, they developed a system of differential equations to describe the behavior of a differential layer in the medium. These results can be integrated over the entire thickness of the medium to describe its behavior. A schematic representation of the setup is shown in Figure 5.
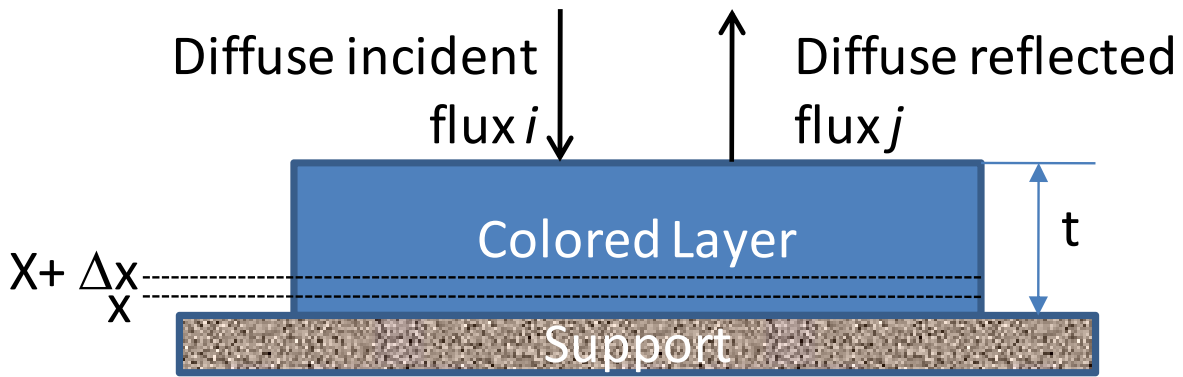
Figure 5. Schematic representation of Kubelka-Munk setup

Several simplifying assumptions were used in Kubelka-Munk theory. They assumed that the material is isotropic and homogeneous but contains scattering centers that are small relative to its thickness. In addition, they assumed that the medium is completely diffuse and reflected light does not have a specular component. In order to avoid boundary effects, surfaces adjacent to the colored layer are assumed to be plane, parallel, and infinite. Spontaneous emission effects such as fluorescence are also neglected in this theory. These assumptions present an obvious limitation to the practical application of this theory, although subsequent modifications (as discussed below) have been proposed to address some of these deficiencies. Despite these limitations, the Kubelka-Munk theory is widely used in the textile industry since it is applicable to opaque media.

The equations that describe the two fluxes in the Kubelka-Munk setup are given in Equation 1 using the variables defined earlier in this section.

$$i_x = i_{x+dx} - i_{x+dx} \cdot (k+s) \cdot dx + s \cdot j_x \cdot dx$$
$$j_{x+dx} = j_x - j_x \cdot (k+s) \cdot dx + s \cdot i_{x+dx} \cdot dx \qquad \text{(Eq 1)}$$

These equations give rise to the fundamental differential equations postulated by Kubelka and Munk, which are summarized in Equation 2.

$$-di = -(k+s) \cdot i \cdot dx + s \cdot j \cdot dx$$
$$dj = -(k+s) \cdot j \cdot dx + s \cdot i \cdot dx \qquad \text{(Eq 2)}$$

Equation 2 represents a simplistic model that assumes all light travels in a path that is perpendicular to the medium. In reality, light can be incident on the medium from any angle and may be incident from many angles at once. As a result, in 1948 Kubelka proposed a modification to the original equations that addressed some of these limitations.[26] The derivation began by considering that the path length through a layer of thickness dx at an angle not perpendicular to the medium would be shown in Equation 3.

$$dx / \cos\theta \qquad \text{(Eq 3)}$$

Based on this variation in path length with angle of incidence, the average path length can be computed using the integral in Equation 4 for the i flux and in Equation 5 for the j flux.

$$d\xi_i = dx \cdot \int_0^{\pi/2} \frac{\partial i}{i \partial \varphi} \cdot \frac{d\varphi}{\cos\varphi} \equiv u \cdot dx \qquad \text{(Eq 4)}$$

$$d\xi_j = dx \cdot \int_0^{\pi/2} \frac{\partial j}{j \partial \varphi} \cdot \frac{d\varphi}{\cos\varphi} \equiv v \cdot dx \qquad \text{(Eq 5)}$$

17

In these equations, the partial derivative describes the angular distribution of those two fluxes. For an ideal diffuser, this angular distribution can be expressed by Equation 6 and via a similar expression for the j flux.

$$\frac{\partial i}{\partial \varphi} = i \sin 2\varphi = 2i \sin \varphi \cos \varphi \qquad \text{(Eq 6)}$$

Substituting Equation 6 into Equation 4 and performing the straightforward integration will demonstrate that u and v both equal 2. Next Kubelka considered the behavior when the thin layer was illuminated by only one of the fluxes at a time.[26] He defined a coefficient of scattering, σ, and coefficient of absorption, ε, and formulated in Equations 7 and 8 this behavior for the i and j fluxes respectively. It should be noted that Kubelka made a simplifying assumption that defines scattering only as occurring in the backward direction from the surface and neglects any forward scattering since that treat.[27]

$$(\sigma + \varepsilon)i d\xi_i = (\sigma + \varepsilon)uidx \qquad \text{(Eq 7)}$$

$$(\sigma + \varepsilon)j d\xi_j = (\sigma + \varepsilon)vjdx \qquad \text{(Eq 8)}$$

Combining Equations 7 and 8 with Equations 4 and 5 and then rewriting in a form similar to Equation 2 leads to a set of differential equations shown in Equation 10. These equations arise from fairly straightforward physical phenomena as the incident radiation is attenuated by reflection and scattering but is augmented by the reflected radiation from the j flux. Similarly, the j flux is attenuated by reflection and scattering but is augmented by reflection from the incident flux.

$$\begin{aligned}
-di &= -(\sigma + \varepsilon) \cdot u \cdot i \cdot dx + \sigma \cdot v \cdot j \cdot dx \\
dj &= -(\sigma + \varepsilon) \cdot v \cdot j \cdot dx + \sigma \cdot u \cdot i \cdot dx
\end{aligned} \qquad \text{(Eq 10)}$$

Since u and v are both equal to the same constant it is possible to substitute $S = u\sigma$ and $K = u\varepsilon$ and rewrite Equation 10 in a similar way as Equation 2 as shown in Equation 11.

$$-di = -(S + K) \cdot i \cdot dx + S \cdot j \cdot dx$$
$$dj = -(S + K) \cdot j \cdot dx + S \cdot i \cdot dx$$

(Eq 11)

These differential equations can be simplified using the following expression:

$$a \equiv \frac{S + K}{S} = 1 + \frac{K}{S}$$

(Eq 12)

Substituting Equation 12 into Equation 11 leads to Equation 13.

$$-\frac{di}{Sdx} = -a \cdot i + j$$
$$\frac{dj}{Sdx} = -a \cdot j + i$$

(Eq 13)

These equations can be rearranged by dividing by i and j respectively and then adding them together. From that form the differential equation can be solved using separation of variables and the result integrated to solve for the reflectance of the medium as shown in Equation 14.

$$R_\infty = 1 + \frac{K}{S} - \sqrt{\left(\frac{K}{S}\right)^2 + \frac{2K}{S}}$$

(Eq 14)

Equation 14 can be reformulated to solve for the K/S ratio in terms of the reflectance of the medium as shown in Equation 15.

$$\frac{(1 - R_\infty)^2}{2R_\infty} = \frac{K}{S}$$

(Eq 15)

This equation is referred to as the Kubelka-Munk function and illustrates why this theory is the most widely utilized of the various theories for diffuse reflectance.[28] Reflectance is a physical

19

property that is easy to measure experimentally, which makes it more applicable in practice. The use of the K/S ratio as opposed to actual values also eases the use of this relation. Finally, the Kubelka-Munk Theory has formed the basis for a number of derivative theories and will therefore be the focus of this analysis.

2.2 Silvy Theory

In 1961 Silvy proposed a particle-based approach that recognized energy exchanges between the medium and the incident light as corresponding to absorption or emission of photons.[23] His approach assumes a homogeneous, non-emitting, dense medium that absorbs much less radiation then it scatters. As with Kubelka and Munk, he assumed that the medium is isotropic and that the incident radiation is monochromatic. This theory recognizes that absorption and emission of photons corresponds to energy exchanges between the medium and its surroundings. Statistics regarding collisions (inelastic collisions for absorption and elastic collisions for scattering) govern this behavior and therefore enable accurate predictions.

The novelty of Silvy's approach is that he simplified the transfer equations and enabled the use of approximations because of the small size of the free paths in the medium relative to the size of the medium. The equation he developed is given in Equation 16.

$$R_\infty = R_\infty(\lambda) = \frac{1 - \left(\frac{4}{3}\Sigma_a/\Sigma_s\right)^{1/2}}{1 + \left(\frac{4}{3}\Sigma_a/\Sigma_s\right)^{1/2}} \qquad \text{(Eq 16)}$$

In Equation 16, the summation terms represent the effective cross section of absorption and the effective cross section of scattering respectively. The similarity between Silvy's result and the Kubelka-Munk equations is fairly obvious and in fact Silvy addressed the similarities in his

20

results by relating the cross section terms he proposed to the K and S terms put forth by Kubelka. These relationships are shown in Equation 17.

$$K = 2\Sigma_a$$
$$S = 0.75\Sigma_s - \Sigma_a \qquad \text{(Eq 17)}$$

It is clear from these relationships that unlike K and S, the effective cross section terms are independent parameters.

2.3 Radiative Transfer Theory

The Kubelka-Munk Theory is actually a very particular case of a more rigorous theory presented by Chandrasekhar in 1950.[29] Radiative Transfer Theory provides a mathematical formulation for the scattering properties of a medium in terms of scattering and absorption coefficients assuming isotropic single scattering. Although this formulation provides the most accurate results, it is often difficult to solve for practical scenarios. As a result, a number of simplifications have been proposed that utilize Chandrasekhar's framework while being more realistic to calculate. Mudgett and Richards have proposed one particularly relevant approach that utilizes a symmetric multiflux model where space is divided into an upper half that contains the backscattered fraction of the incident radiation and a lower half that holds the fraction diffused in the direction of incidence.[30] This arrangement allows the use of as many fluxes as desired in each of these spaces.

21
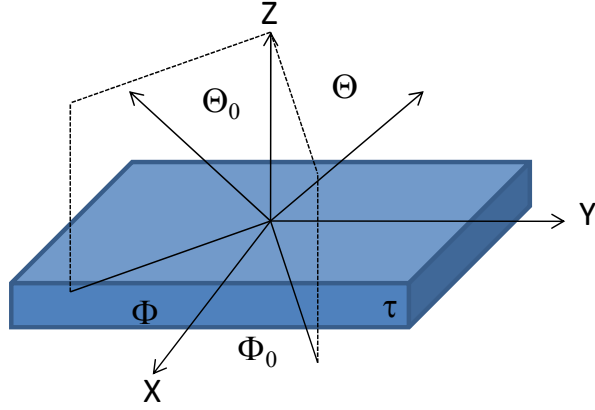
Figure 6. Geometry for radiative transfer equations

The basic geometry for the radiative transfer equations is depicted graphically in Figure 6. In this setup, Θ_0 represents the angle between the incident radiation and the z-axis that is normal to the surface and ϕ_0 is the azimuth angle about the z-axis for the incident radiation. Similarly, Θ represents the angle between the reflected radiation and the z-axis that is normal to the surface and ϕ_0 is the azimuth angle about the z-axis for the reflected radiation. The optical thickness of the surface is represented by τ. In order to simplify the equations further, the cosine of Θ is represented by μ. These variables are used to form the basic equation that describes the radiance I as a function of τ, μ, and ϕ where p is the phase function for the scattered light: [31]

$$\mu\frac{dI(\tau,\mu,\phi)}{d\tau} = I(\tau,\mu,\phi) - \frac{1}{4\pi}\int_{-1}^{1}\int_{0}^{2\pi} p(\mu,\phi,\mu',\phi')I(\tau,\mu',\phi')du'\,d\phi' \qquad \text{(Eq 18)}$$

This equation applies to a broad range of radiation and is not confined merely to visible light, which increases its utility greatly. In addition, it can be simplified further by considering only the flux that penetrates to the thickness of the surface ($\pi\Phi e^{-\tau/\mu}$) and the corresponding diffuse radiation field. This modifies Equation 18 to the following: [31]

22

$$\mu \frac{dI(\tau,\mu,\phi)}{d\tau} = I(\tau,\mu,\phi) - \frac{1}{4\pi} \int_{-1}^{1} \int_{0}^{2\pi} p(\mu,\phi,\mu',\phi') I(\tau,\mu',\phi') du' d\phi' - \frac{1}{4} \Phi p(\mu,\phi,-\mu_0,-\phi) e^{-\tau/\mu_0}$$

(Eq 19)

Further simplification is possible by defining an albedo; ω, which is the ratio of the scattering coefficient for the surface to the sum of its scattering and absorption coefficients, and also by assuming that the surface is isotropic and therefore scatters equally in all directions. With these modifications, Equation 19 reduces to: [31]

$$\mu \frac{dI(\tau,\mu)}{d\tau} = I(\tau,\mu) - \frac{\omega}{2} \int_{-1}^{1} I(\tau,\xi) d\xi - \frac{1}{4} \Phi \omega e^{-\tau/\mu_0}$$

(Eq 20)

For a surface with a known optical thickness, Equation 20 can be solved for τ equal to zero for the reflected radiance and equal to its maximum value for the transmitted radiance. These solutions are shown in Equation 21 for the transmitted radiance and Equation 22 for the reflected radiance. [31]

$$I(\tau,-\mu,-\mu_0) = \frac{1}{4} \Phi \omega \frac{\mu_0}{\mu - \mu_0} [Y(\mu)X(\mu_0) - X(\mu)Y(\mu_0)]$$

(Eq 21)

$$I(0,\mu,\mu_0) = \frac{1}{4} \Phi \omega \frac{\mu_0}{\mu + \mu_0} [X(\mu)X(\mu_0) - Y(\mu)Y(\mu_0)]$$

(Eq 22)

In these equations X and Y represent integral equations that are functions of optical thickness, the albedo, and the cosine of the incidence angle and are solved using iterative methods or tables. For the limiting case where the optical thickness goes to infinity, the Y function reduces to zero while the X function is equal to H(μ) where H is a nonlinear integral equation:

$$H(\mu) = 1 + \frac{1}{2} \omega \mu H(\mu) \int_{0}^{1} \frac{H(\xi)}{\mu + \xi} d\xi$$

(Eq 23)

23

As with the X and Y functions, the H function can be numerically estimated using an iterative procedure, tables have been developed for easy reference using this procedure.[32] For the case of a semi-infinite slab of scattering material (which is representative of textile materials) the reflected radiance can then be described through the following equation:

$$I(0,\mu,\mu_0) = \frac{1}{4}\Phi\omega\frac{\mu_0}{\mu+\mu_0}H(\mu)H(\mu_0)$$
(Eq 24)

Using this result, the radiance factor β for illumination assuming the incidence angle and viewing direction defined earlier for diffuse radiation is given by the following expression:

$$\beta(\mu) = 1 - H(\mu)\sqrt{(1-\omega)}$$
(Eq 25)

The mathematical complexity required to solve the radiative transfer equation for practical applications [33] has led to the development of a number of approximations that are suitable for particular conditions.[34-36] Of particular interest for modeling the diffuse reflectance of textile materials is the semi-infinite slab approximation that was discussed previously. In that case, the Y function approaches a limit of zero while the X function approaches the value of the H function. The H function value can be approximated using a two flux assumption using the following expression:

$$H(\mu) = \frac{1+2\mu}{1+\lambda\mu}$$
(Eq 26)

Where the expression for lambda is:

$$\lambda = 2\sqrt{1-\omega}$$
(Eq 27)

While the exact values for H can only be obtained either from the tables published by Chandrasekhar or by iterative numerical calculations, this approximation has been demonstrated

to provide good agreement, particularly for lower albedo values.[37] This comparison also holds true for computation of the radiance factor, with lower albedo values providing closer agreement to the approximations. These approximations can then be compared to the reflectance values predicted by the Kubelka-Munk Theory by relating the K/S ratio defined by Kubelka and Munk to the albedo defined in radiative transfer theory. This relationship is described by the following equation which includes a factor of four to correct for a slightly different definition of that ratio in the radiative transfer setup compared to the Kubelka-Munk theory.

$$K/S = \frac{4}{\omega} - 4 \qquad \text{(Eq 28)}$$

The reflectance of the material was previously defined by Kubelka and Munk as a function of this ratio:

$$R_\infty = 1 + \frac{K}{S} - \sqrt{\left(\frac{K}{S}\right)^2 + \frac{2K}{S}} \qquad \text{(Eq 14)}$$

Equation 28 can then be substituted into Equation 14 and then simplified as follows:

$$R_\infty = 1 + \frac{4}{\omega} - 4 - \sqrt{\left(\frac{4}{\omega} - 4\right)^2 + 2\left(\frac{4}{\omega} - 4\right)} \qquad \text{(Eq 29)}$$

$$R_\infty = \frac{4}{\omega} - 3 - \sqrt{\frac{16}{\omega^2} - \frac{32}{\omega} + 16 + \frac{8}{\omega} - 8} \qquad \text{(Eq 30)}$$

$$R_\infty = \frac{4}{\omega} - 3 - \sqrt{\frac{16}{\omega^2} - \frac{24}{\omega} + 8} \qquad \text{(Eq 31)}$$

Comparison of the reflectance values predicted by Equation 31 with those predicted by the rigorous radiative transfer equation indicated good agreement, particularly for high albedo

values.[31] This demonstrates that the Kubelka-Munk approach is a useful approximation to a full radiative transfer solution.

One additional consideration is necessary to account for the difference in index of refraction between air and the textile material. This difference leads to reflections off the surface of the material where the incident light does not interact with the fibers and pigments within the textile. Because the radiative transfer theory assumes that the index of refraction is the same for the textile material as for the surrounding medium, modifications are required to address these conditions. These modifications start with Snell's Law, formulated in terms of the variables defined for the radiative transfer geometry and assuming that the index of refraction for air is 1:

$$1 - \mu_1{}^2 = n^2 \left(1 - \mu_2{}^2\right) \qquad \text{(Eq 32)}$$

The subscripts in Equation 32 refer to the medium where 1 represents air and 2 represents the textile. Snell's Law is then used to modify the radiance factor described in Equation 25 to create an observed radiance factor that incorporates the radiance factor that might be seen just inside the surface of the medium to explain the radiance factor that might be seen experimentally. For a case involving diffuse radiation, the resulting equation is:

$$\beta_{obs}(\mu_1) = r(\mu_1) + 2[1 - r(\mu_1)] \int_0^1 t(\mu_{02}) \beta^*(\mu_2, \mu_{02}) \mu_{02} d\mu_{02} \qquad \text{(Eq 33)}$$

Where:

$$r(\mu_1) = \frac{1}{2} \left[\left(\frac{a_1 - \mu_1}{a_1 + \mu_1} \right)^2 + \left(\frac{n^2 \mu_1 - a_1}{n^2 \mu_1 + a_1} \right)^2 \right] \qquad \text{(Eq 34)}$$

$$a_1{}^2 = n^2 - \sin^2 \theta_1 \qquad \text{(Eq 35)}$$

$$n = \frac{n_2}{n_1} \qquad \text{(Eq 36)}$$

$$t(\mu_{02}) = 1 - r(\mu_{02}) \qquad \text{(Eq 37)}$$

In this setup, β^* is the radiance factor just below the surface of the medium and is related to the

radiance factor in Equation 25 by the following expression: [31]

$$\beta^*(\mu_2, \mu_{02}) = \beta(\mu_2, \mu_{02}) + 2\int_0^1 \beta^*(\xi, \mu_{02})r(\xi)\beta(\mu_2, \xi)\xi d\xi \qquad \text{(Eq 38)}$$

Here ξ is a variable of integration; μ_2 and μ_{02} represent the cosines of the angle of incidence and

reflection respectively inside the surface of the textile material, and r is the Fresnel reflectance of

that material's surface. For a diffuse reflector, an additional simplification can be made by

assuming that β^* is constant and independent of both the angle of incidence and angle of

reflection. In that case, Equation 33 reduces to:

$$\beta_{obs}(\mu_1) = r(\mu_1) + \left[1 - r(\mu_1)\right]\left[1 - 2\int_0^1 r(\xi)\xi d\xi\right]\beta^* \qquad \text{(Eq 39)}$$

Given the assumption that β and β^* are constant, the solution to Equation 38 becomes:

$$\beta^* = \frac{\beta}{1 - C_1\beta} \qquad \text{(Eq 40)}$$

Equation 40 can be used to simplify Equation 39:

$$\beta_{obs}(\mu_1) = \left[C_2 + (1 - C_2)\right]\cdot\left[\frac{(1 - C_1)\beta}{1 - C_1\beta}\right] \qquad \text{(Eq 41)}$$

Where the two constants are defined by the following expressions:

27

$$C_1 = 2\int_0^1 r(\xi)\xi d\xi \qquad\qquad\qquad\qquad \text{(Eq 42)}$$

$$C_2 = r(\mu_1) \qquad\qquad\qquad\qquad\qquad \text{(Eq 43)}$$

These expressions describe the Fresnel reflectance of the surface and are dependent on the indices of refraction for both the sample and the surrounding medium as well as the viewing geometry. Although these results have been obtained using simplifying assumptions, non-ideal cases exist where constant radiance factors as a function of viewing geometry cannot be assumed occur frequently in nature. In those situations, the radiance factor can be computed numerically using several different techniques; however these approaches are all computationally intensive and much less desirable than the solution obtained using simplifying assumptions. The importance of correcting for surface reflections has been illustrated by several analyses that compare the accuracy of both radiative transfer and Kubelka-Munk solutions obtained with and without correcting for surface reflections. These analyses demonstrated that neglecting the change in index of refraction that occurs at the boundary between air and the textile medium results in a substantial difference in the final results. [37]

The general behavior that has been observed is that Kubelka-Munk performs very well for higher albedo values, particularly when the correction for surface reflections has been included in the calculations. Approximations of the radiative transfer result, particularly the two flux approximation, exhibit the reverse behavior, with their best agreement occurring at lower albedo values. Despite some deviations, both techniques provide generally good agreement for all albedo values for most applications, and therefore the exact solution is required only when high accuracies are required. Applying a correction for surface reflections is important for all techniques, including the exact solution, and should be performed whenever possible. It is

important to note that these approaches have been tested primarily in the visible portion of the spectrum based on the current literature. The experimental portion of this effort will test the applicability of Kubelka-Munk in the SWIR spectrum, particularly to explain phenomenology that has been observed in SWIR imagery. [20]

3   Experimental Approach

Recent advances in detector technology have made SWIR imaging systems available with sensitivities sufficiently high to support reasonable signal to noise ratios under starlight conditions. This capability has enabled a variety of experiments to be performed to characterize human observer performance using sensors operating in this waveband. One of the first observations made using these sensors was that the appearance of human targets in SWIR imagery differs significantly from typical visible band imagery.[20] These differences include hair (which generally appears bright in the SWIR), skin (which generally appears dark), and clothing. It was quickly apparent that the presence of moisture in the target surface had a significant impact on appearance in the SWIR band. This was not surprising given the strong absorption by water in the SWIR band, particularly when compared to the visible band, as shown in Figure 7. [38]
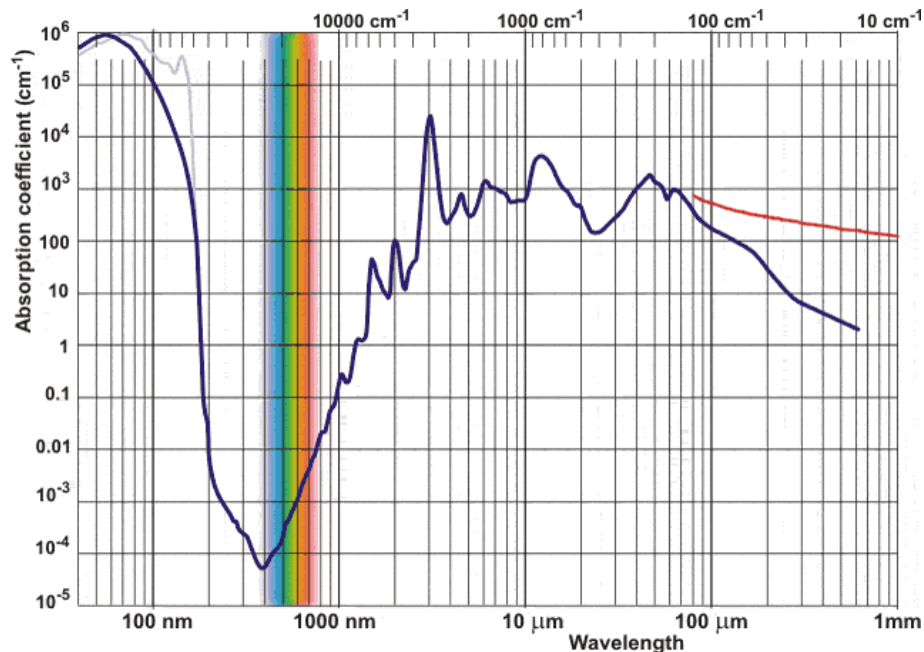
Figure 7. Absorption spectrum for water [38]

Specific water absorption lines occur at 970 nm, 1200 nm, and 1470 nm where the frequency of the incident light matches vibrations of the O-H bonds in the water.[39] As a result, high moisture content leads to increased absorption of incident SWIR radiation, which is responsible for the darker appearance of surfaces such as human skin and foliage that have significant water content. This effect also leads to another interesting observation regarding the effectiveness of camouflage clothing that has been designed to blend into foliage backgrounds. Since the moisture content of textile fabrics is generally less than the moisture content of naturally occurring foliage, clothing typically takes on a uniform brighter appearance in the SWIR as illustrated in Figure 8. Of particular note is that the appearance is largely independent of the camouflage pattern dyed on the hat, which renders the camouflage largely ineffective, particularly against a dark foliage background. [40]
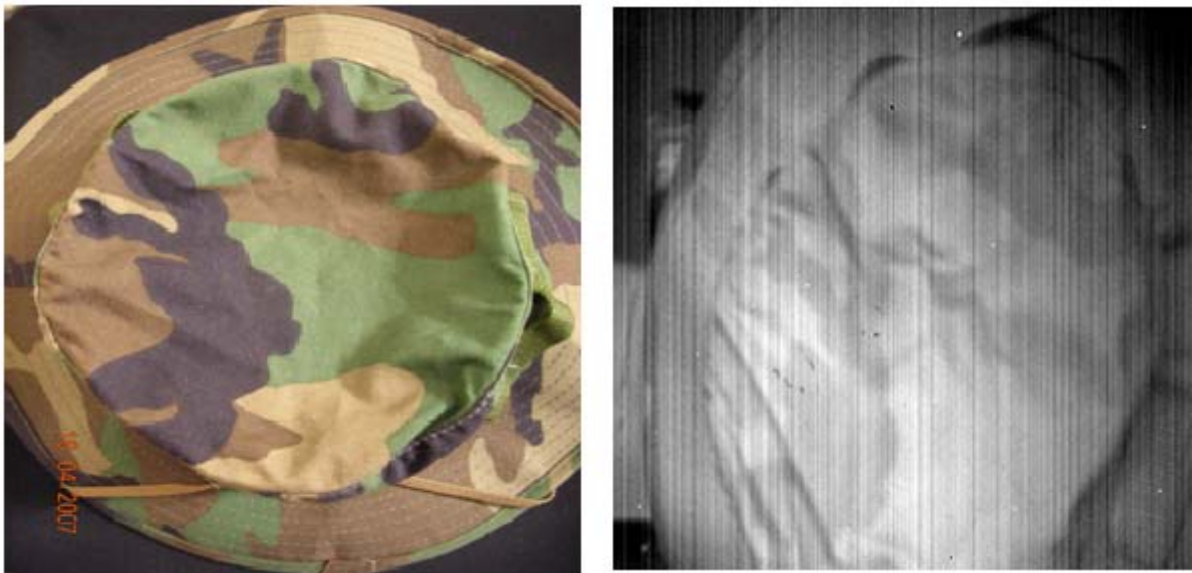
Figure 8. Visible and SWIR imagery of camouflage hat [40]

An additional SWIR image of a human target against a foliage background under daylight conditions is shown in Figure 9 illustrates the uniformly high reflectance of the person relative to the vegetation in the background. Although the results are not always as dramatic as in these figures, it is clear from observation that there are significant differences in the diffuse reflectance behavior of dyed textiles in the SWIR as compared to the visible band. Furthermore, there are some fabrics that have the same uniform appearance but with a much lower apparent reflectance. The experimental approach described here was designed to help quantify these observations and support an analysis of possible explanations for the reflectance behavior of textile materials.

Figure 9. SWIR image of person against foliage background [40]

3.1 Sample Set

A set of fabric test articles was developed to support the experimental effort. In order to minimize the number of variables being tested simultaneously, two common textile fabrics – cotton and polyester – were selected and only samples containing 100% concentrations of each

fabric were used. In addition to being common fabrics for clothing, cotton is a natural fiber while polyester is man-made, which lends an additional degree of diversity to the sample set. All of the samples were commercially available fabrics and with different dye types, concentrations, and patterns. The visual appearance of the fabrics was classified into three general categories. Solid fabrics were uniformly dyed with a single color over the entire sample. Striped fabric samples were dyed with periodic patterns such as stripes, dots, or similar features comprised of multiple different dyes. Patterned fabric samples contained many different dyes as arranged in complex graphical designs throughout the sample. This set of fabric samples represents the scope of real world fabric appearances in clothing articles and also contains the two most common textile materials used in clothing. As a result, this is a very diverse set of samples that was specifically selected to provide insight into the phenomenology of diffuse reflectance for textiles in the SWIR.

Cotton is a naturally occurring fiber that originates from plants in the tropical and subtropical parts of the world. It is harvested and processed to remove a variety of impurities which results in a fiber that consists primarily of cellulose and water. Following this processing, the fibers form into an interlocked form that is optimal for creating the fine yarn needed for making cloth. This, in addition to the soft, breathable, feel has made cotton the most common textile fiber in the world today with a market share of 56% [41] for all apparel and home furnishings in the United States. Table 2 contains typical values for the physical properties of cotton.

Table 2. Properties of cotton fibers [42]

Property		Value
Shape	Length	1-6 cm (2.2 cm average)
	Width	12-20 microns
Luster		Low
Tensile Strength	Dry	3.0 – 4.9 g/denier
	Wet	3.3 – 6.0 g/denier
Resiliency		Low
Density		1.54 – 1.56 g/cm3
Moisture Absorption		7.0 – 11.0 %

The term polyester actually refers to a class of polymers that contain the ester functional group in their main chain, but most commonly is used to describe the material polyethylene terephthalate (PET).[43] PET polyester is a synthetic fiber that is popular for clothing since it has low moisture absorption and is considered to be very durable for consumer applications. Polyester is a particularly versatile fiber that is a combination of Terephthalic Acid or Dimethylterephthalate and Ethylene Glycol. It is commonly produced via melt spinning and takes on a white color when not dyed. There are a number of methods for manufacturing PET fibers which are suitable for different applications, but the synthetic nature of the fibers allows them to be manufactured in a wide variety of diameters and lengths. As a result, PET polyester fibers are produced as multifilament or monofilament yarns with a wide range of counts and staple lengths to suit any type of textile requirement.[43] Table 3 is a summary of the key physical properties of PET polyester fibers. Cotton is a denser material than polyester with a density of 1.54 – 1.56 g/cc versus 1.22-1.38 for typical polyester fibers. It also absorbs moisture at a much greater rate than polyester, with a moisture regain range of 7% – 11% versus 0.4% – 0.9% for polyester. Moisture regain is a measure of the moisture present in a material as a percentage of the moisture-free weight at 70 deg F and 65% relative humidity. [44]

Table 3. Properties of polyester fibers [44]

Property		Value
Shape		Cylindrical – Diameter can vary widely
Luster		High
Tensile Strength	Dry	2.0 – 4.0 g/denier
Resiliency		High
Density		1.22 - 1.38 g/cm3
Moisture Absorption		0.4 – 0.9 %

A total of 96 samples were tested during the experimental portion of this work, 52 of which were 100% cotton and 44 of which were 100% polyester.

3.2 Instrumentation

Measurements of diffuse spectral reflectance can be made using a variety of techniques, each with different advantages and disadvantages.   The three major functional subsystems of a spectrophotometer include the light source, the detector, and its optical configuration.   Optical configuration is perhaps the most variable design element, particularly as far as mechanisms for spectrally separating the light being measured. Options for dispersing light include:[45]

- **Diffraction Gratings (Fixed or Movable)**
- Interferometers
- Interference Filters
- Prisms
- Spectrally-Narrow LEDs
- Tunable Filters (Acousto-Optical, Liquid Crystal)

The optical configuration that is ultimately utilized for a particular application depends largely on the specific measurement requirements. For instance, an instrument using interference filters may be rugged and low cost, but cannot provide the spectral resolution or calibration accuracy of an instrument that uses a diffraction grating. A wide range of light sources can also be used,

depending on the spectral region being measured. Source options include the following (with candidates for use in the SWIR shown in bold): [45]

- Deuterium Arc Lamp
- Xenon Flash Lamp
- **Tungsten-Halogen Lamp**
- LEDs
- **Tunable Laser**
- **Globar**
- Nichrome Wire
- **Quartz Halogen Lamp**
- Mercury Vapor Lamp

Numerous detector options are available as well, with the primary driver being the need for sensitivity in the spectral region being measured. In addition, the noise characteristics of the detector must be matched to the light source, optical configuration, and behavior of the samples that are being measured. A sampling of potential detector types includes the following (with candidates for use in the SWIR shown in bold): [45]

- Photomultiplier Tubes
- Silicon Photodiodes (190 nm - 1100 nm)
- Germanium Photodiodes (400 nm – 1700 nm)
- **PbS/PbSe Photodiodes (1000 nm – 3500 nm)**
- **InGaAs Photodiodes (800 nm – 2600 nm)**
- InSb Photodiodes (1500 nm – 5500 nm)
- Thermisters/Thermocouples

There are also a number of other design issues that must be considered, including the scan rate for the device, environmental conditions (dust, ambient light, etc), vibration tolerance, and desired sample geometry.

Table 4. Specifications for spectrophotometers

Specification	Explanation
Wavelength Range	Total usable spectral range for the device, including light source, optics, and detectors.
Spectral Resolution	The width of the spectral region over which the property being measured was averaged. For a grating instrument, this is the convolution of the dispersion of the grating and the slit width.
Wavelength Accuracy	Measure of the difference between the reported wavelength for each data point and the actual wavelength as determined by a NIST-traceable standard.
Photometric Accuracy	Difference between the measured photometric measurement (transmittance, reflectance, absorptance, etc) and the absolute value of that property for the sample.
Baseline Flatness	Spectrophotometers are baselined prior to use with a reference scan to account for the intrinsic behavior of the source, optics, and detectors.
Stray Light	Since no dispersive element can block 100% of the out of band light, this is a measure of the amount of light from other wavelengths that reaches the sample and detector. Excessive stray light can lead to significant measurement errors and is controlled through good optical design.
Scan Speed	Time required to perform a complete measurement over the selected spectral range and at the selected spectral resolution.

The basic methodology for measuring reflectance with a spectrophotometer is shown in Figure 10 for a so-called 0/45 configuration where the sample is illuminated at normal incidence and the reflectance is measured at 45 degree angles. In this approach, the output from a light source emitting in the spectral band of interest (deuterium for UV and tungsten-halogen for VIS/SWIR) is incident on the entrance slit to a grating monochromator. The light passing through the entrance slit is then collimated and diffracted by the grating, with the resulting light reimaged onto the exit slit of the device. By rotating the diffraction grating, the user can mechanically select the narrow spectral band of light that is transmitted through the exit slit.

37

Order sorting filters are used to eliminate higher order diffractive effects that would otherwise result in the transmission of out of band light. The resulting monochromatic light is then incident on the sample, which reflects some portion to the two detectors located at 45 degree angles. These detectors then output a signal to a low noise, high-gain amplifier followed by an analog to digital converter. The digital signal is recorded by a computer and stored for analysis. The process is repeated twice for the wavelength range and spectral resolution selected by the user – once with the sample under test and once with a reference sample of known reflectance. This reflectance sample is generally a material such as Spectralon that has a very uniform high reflectance that is flat across a broad spectral region. The control computer is used to control the entire process by orchestrating the motion of the grating, selection of the sources and detectors, insertion and removal of order sorting filters, and acquisition of data.
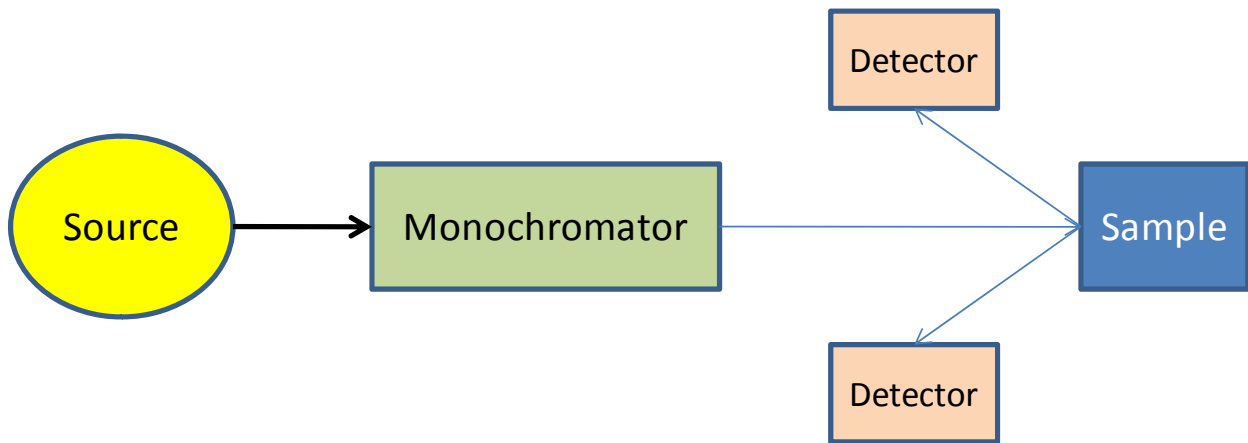
Figure 10. Basic configuration for measuring reflectance

Relative reflectance measurements are most commonly used in spectrophotometers and require a well calibrated reference standard for reliable results. These can be configured in either substitution mode, where the sample and reference are tested alternately, or comparison mode, where the sample and reference are installed simultaneously and are tested through mechanical manipulation. The substitution mode represents the simplest design since no moving parts are

required and is therefore used in most modern spectrophotometers. In this configuration, three

measurements are required for each sample – one of the sample itself, one of the reference

standard, and a baseline measurement with nothing installed in the sample holder. This baseline

is needed to correct for the varying spectral throughput of the various components in the system,

particularly the efficiency of the diffraction grating.

Table 5. Cary 5E key components

Component	Cary 5E Specification
UV Light Source	Deuterium
VIS/SWIR Light Source	Tungsten-Halogen
UV/VIS Detector	R928 Photomultiplier Tube
SWIR Detector	Cooled PbS
Dispersion Mechanism	Diffraction Grating

Figure 11. Cary 5E spectrometer used in these experiments

Given all of these considerations, the instrument used for these measurements was a Cary

5E (shown in Figure 11) double-beam, double-grating spectrophotometer with a wavelength

range of 175 nm to 3300 nm. A summary of the key components in the Cary 5E is shown in

Table 5. Two light sources - deuterium (UV) and tungsten-halogen (VIS/SWIR) lamps - are

installed in the instrument, although mercury and other lamps can be substituted in the source

turret. Light from the sources is collected using Schwarzchild source optics that are positioned

next to the turret and which direct the light through an aperture to ensure that the grating is under-filled, which minimizes stray light. These optics are optimized to avoid aberrations and have a large collection angle to maximize collection efficiency. Just prior to the monochromator is a filter wheel that is used to limit the spectral region of the incident light in order to avoid higher order diffraction effects at the grating. This filter wheel contains six different filters that are selected automatically by computer in conjunction with the scan wavelength. Following the filter wheel, the light passes through the entrance slit to the monochromator and is incident on a collimating mirror that reflects it onto the grating. There are two gratings installed in the instrument on a rotating mount: one is a UV/VIS grating that covers 175 nm to 800 nm and the other is a SWIR grating that covers 800 nm to 3300 nm. The correct grating is automatically selected by computer as the measurement is performed. Key specifications for the two gratings are shown in Table 6.

Table 6. Cary 5E monochromator grating parameters

Specification	UV/VIS Grating	SWIR Grating
Grating Size	70 x 45 mm	70 x 45 mm
Blaze Angle	8.5	10.3
Blaze Wavelength	250 nm	1192 nm
Reciprocal Dispersion	0.98 nm/mm	3.92 nm/mm
Lines per mm	1200 lines/mm	300 lines/mm

Following the first grating, the light strikes the collimating mirror again and then passes through an intermediate slit before reaching a second monochromator that is identical to the first. The second monochromator serves to cancel any aberrations induced by the first grating and also to minimize any remaining stray light. Following the second grating, the light is directed to the exit slit and then on to the sample area. The size of this exit slit determines the spectral bandwidth of the instrument.

The scanning capability of the Cary 5E is achieved by rotating the monochromator gratings about their centers, which changes the wavelength of the light incident on the exit slit. When the user selects the spectral range of interest, that determines the angular rotation required for each grating. In early spectrometers measurements were performed continuously as the grating rotated, which led to errors since the sample and reference beam measurements were not performed at the same wavelength and also led to averaging over multiple wavelengths. The Cary 5E uses discrete measurements where movement of the grating occurs only during the non-measurement phase of the chopper cycle. This requires the grating to remain at a discrete wavelength for as long as necessary to perform measurements using both the sample and reference beams. In addition, the rotation of the grating must be performed very rapidly to occur only during the non-measurement phase of the chopper. This requirement is met using a high speed stepper motor controlled by a microprocessor to minimize vibration and backlash.

After passing through the exit slit, the light enters a chopper compartment where it is divided into the required sample and reference beam. The chopper wheel contains three sections: a mirrored blade that reflects the beam into the sample compartment, a matte black blade that allows correction for dark current, and an open section through which the reference beam passes. The optics in the chopper compartment image the grating onto the chopper and then again onto the detector to minimize sensitivity to chopper vibration and also ensure that the beam projection on the detector is invariant to spectral bandwidth. The detectors are an R928 UV-enhanced photomultiplier tube (PMT) and a cooled lead sulfide cell. The instrument self-calibrates in wavelength on every initialization using the deuterium lamp.

The sample compartment is large and flexible and can support a number of different measurement configurations, including transmittance, absorptance, and reflectance. Diffuse reflectance is measured using a specialized diffuse reflectance accessory (DRA), shown in Figure 12, installed in the sample compartment in the Cary 5E. The DRA uses a 110 mm diameter Polytetrafluoroethylene (PTFE) coated integrating sphere with internal PMT and PbS detectors, and is usable within the wavelength range from 250 to 2500 nm. PTFE is a good uniform reflectance coating in that wavelength range, with typical reflectance values greater than 99% between 350 nm and 1800 nm.
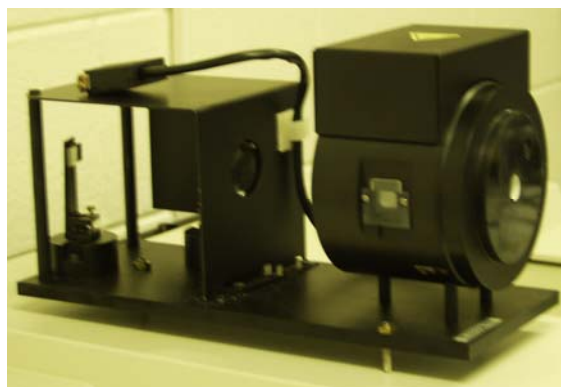
Figure 12. Diffuse reflectance accessory for Cary 5E

The DRA uses the substitution method for diffuse reflectance measurements and includes a PTFE reference standard that can be inserted in the sample port. The optical design is shown in Figure 13 and can be described as follows:

1. The sample beam hits mirror M1 and is then reflected to M2.

2. The beam travels through the lens and is focused into the entrance port, and onto the sample port.

3. The reflected beam is diffused throughout the sphere before being measured by the detector.

4. The reference beam enters the sphere directly through the reference port and is dispersed.

5. The removable end cap has two positions:

42

a. In the 'D' position, the angle of the beam from the normal to the sample plane is approximately 0° degrees. Any specular component of the reflection is reflected back through the entrance port and is deflected by the angled lens, preventing re-entry into the sphere.

b. With the cap in the 'S' position, the angle of incidence is 3° 20 min. The specular component will hit the sphere wall and be diffused within the sphere. The total reflectance will then be measured.
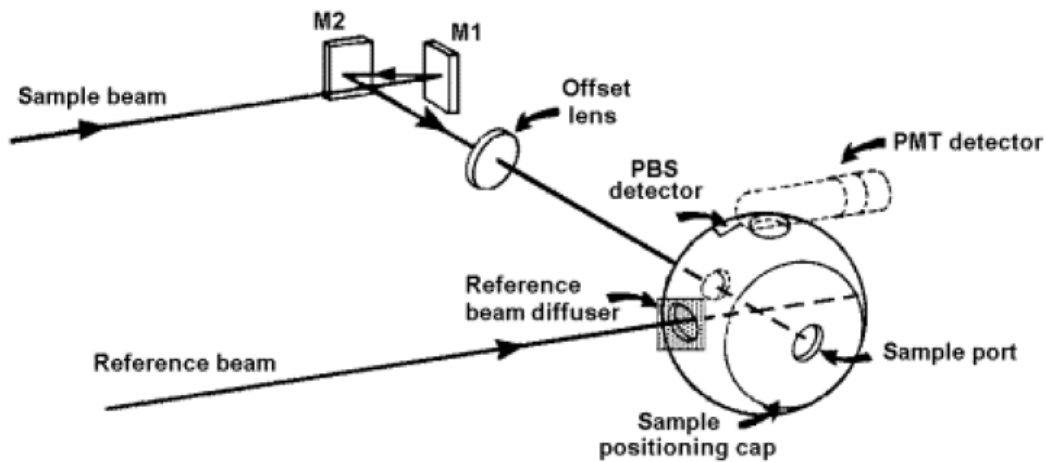
Figure 13. Optical design of the Cary 5E DRA

3.3 Measurement Procedure

Diffuse reflectance measurements were made for each of the fabric samples described previously using the Cary 5E spectrophotometer with the diffuse reflectance accessory installed as shown in Figure 14.
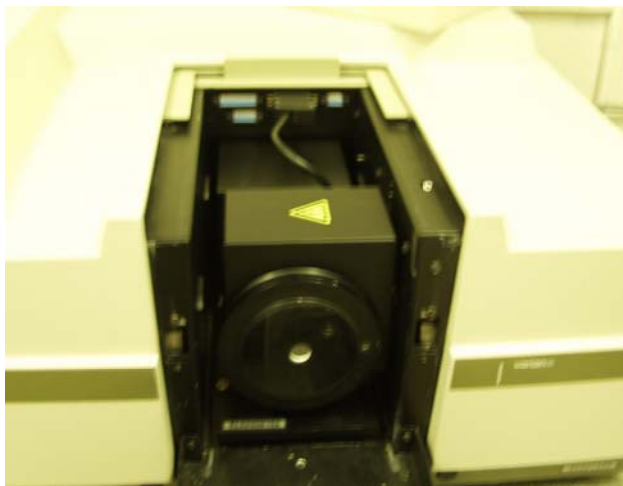
Figure 14. DRA installed in Cary 5E sample compartment

The process to perform the measurements is fairly straightforward but requires the user to exercise care to ensure proper installation of the sample in the sample holder. The samples in this experiment came in two size variants – 2" x 2" and 8" x 8". The smaller samples fit directly in the sample holder while the larger samples required manipulation to handle the excess material. Once the sample was properly installed as shown in Figure 15, the following procedure was followed:

- Experimental parameters on the Cary software were set to a wavelength range of 400 to 2000 nm with an interval of 1 nm.

- The "Baseline" method was set to Zero/Baseline" correction

- Inserted the reference sample comprised of a Lambertian Spectralon coating with near 100% reflectance across the whole spectral region and recorded the baseline measurement.

- Removed the reference sample and, leaving the sample holder empty, recorded a zero reference baseline was collected.

- The test article was then installed in the sample holder and its spectrum was recorded by the spectrophotometer.

- The spectrophotometer software calculates the calibrated reflectance spectrum for the sample, accounting for both the reference and zero baselines automatically. The result is saved in CSV files that can be easily manipulated using other software.

Figure 15. Sample installed in DRA

4   Results and Analysis

The reflectance of each fabric sample in the test matrix was measured using the Cary 5E spectrometer in accordance with the procedure described in the previous section. The reflectance spectrum for each sample was measured from 400 to 2500 nm with a resolution step of 1 nm. A total of 96 samples were measured of which 52 were cotton swatches and 44 were polyester swatches. Each swatch fell into one of three general categories (art, patterned, solid) that qualitatively described its appearance. Swatches in the art category included complex, multi-color images on the sample while swatches in the patterned category included simpler recurring features such as stripes or dots. Solid swatches included a single color and had a texture that was characteristic of the component textile fabric. A detailed breakdown of the sample counts by fabric type and category is shown in Table 7. Appendix A contains a complete listing of the samples, including material, category, visible color description, and identification numbers.

Table 7. Sample counts by material and type

Classification	Cotton	Polyester	TOTAL
Art	25	10	35
Patterned	16	8	24
Solid	11	26	37
TOTAL	52	44	96

The accumulated reflectance data for all 96 samples is shown below in Figure 16 for cotton samples and Figure 17 for polyester samples. Inspection of this data immediately leads to several noteworthy observations. First, the reflectance data in the visible spectral region between 400 nm and 700 nm has a significant amount of structure that makes it difficult to ascertain any trend between the various samples or between the cotton and polyester cohorts.
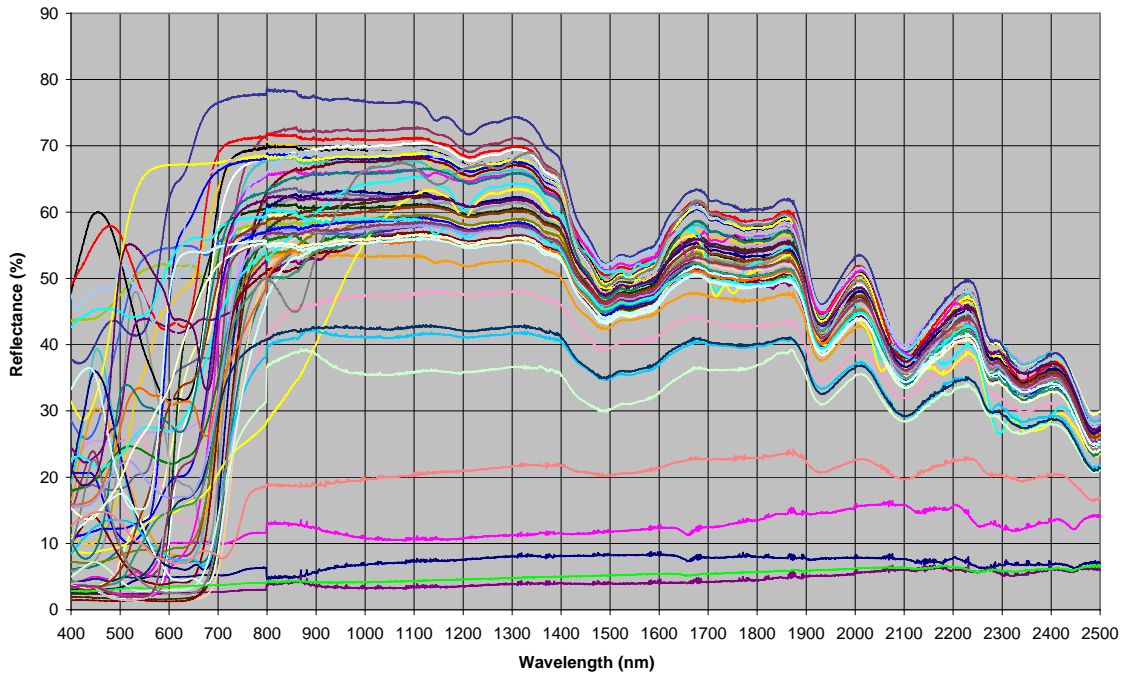
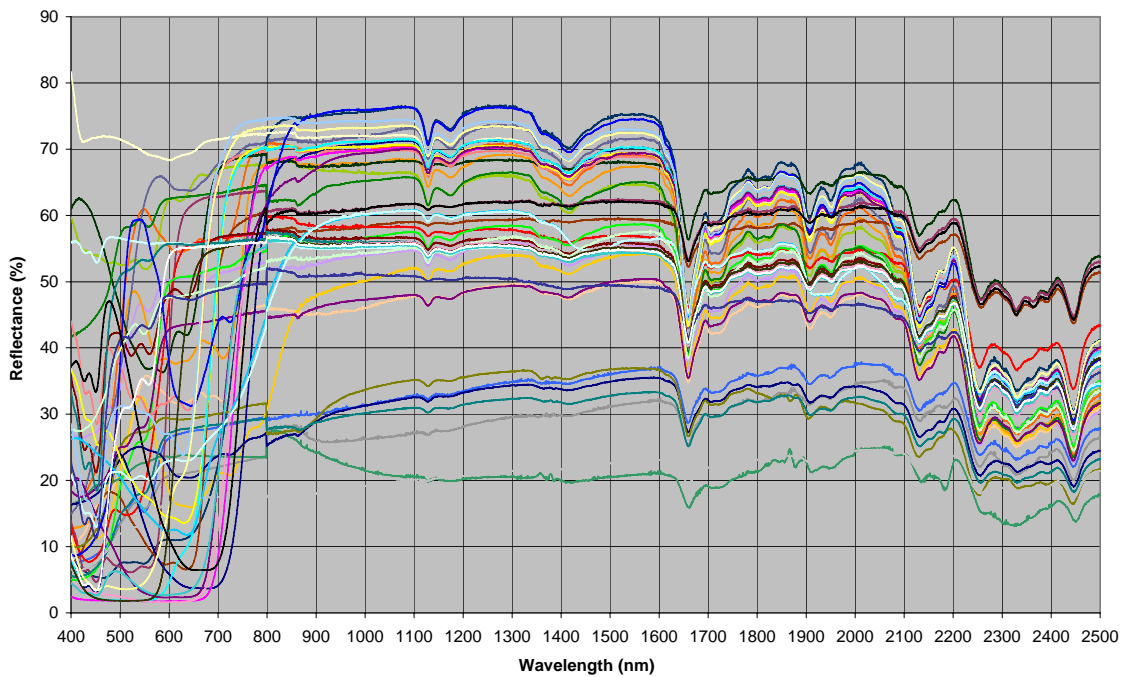Figure 16. Measured spectral reflectance for cotton samples

Figure 17. Measured spectral reflectance for polyester samples

However, between 700 and 900 nm, the reflectance tends to increase for both sample types and
then becomes fairly uniform throughout the SWIR imaging band (900 nm to 1700 nm,
corresponding to lattice-matched InGaAs detectors) with a reflectance value in the range

47

between 50% and 70%. In both cases, but especially in the cotton cohort, there are also several outlying samples that have significantly lower reflectance values throughout the SWIR region as compared to the mean reflectance values.

These observations led to several questions that are essential to understanding the diffuse reflectance behavior of these fabrics. The behavior of the outlying cases in the SWIR region needs to be better understood since those cases would serve as an impediment to a standard model for behavior in that spectral region. In addition, the variation in reflectance with wavelength for both cotton and polyester needs must be assessed further. Finally, the difference in average reflectance between polyester and cotton samples needs to be explored further.

The first step in addressing these issues was to consider the impact of the qualitative appearance of each sample swatch on the reflectance measurements. It was immediately apparent that the outlying samples were in the "Art" category and included extensive combinations of colors, patterns, and other physical features. Some of these patterns used low density fabric weaves that resulted in significant transmission through the fabric sample, which in turn decreases the reflectance measured by the spectrometer. In order to quantify this behavior, the samples that were classified as solid were analyzed separately. Reflectance spectra from the 11 cotton samples and 26 polyester samples classified as solid were considered separately from the other samples. These plots are shown below in Figure 18 for cotton samples and Figure 19 for polyester samples. It is readily apparent from these plots that the outliers have been eliminated, which confirmed the initial hypothesis that the outlying cases were due to the fabric construction needed to accommodate the graphics displayed on those samples and were not associated with a fundamental material property.
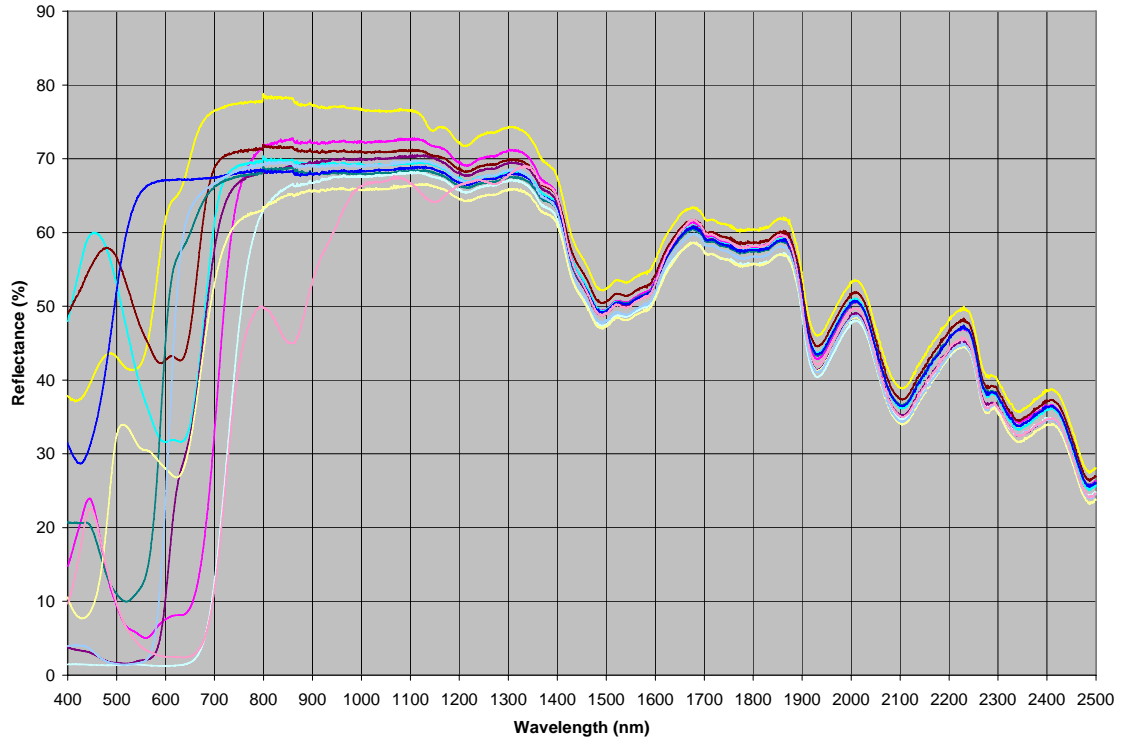
Figure 18. Reflectance spectra for solid cotton samples
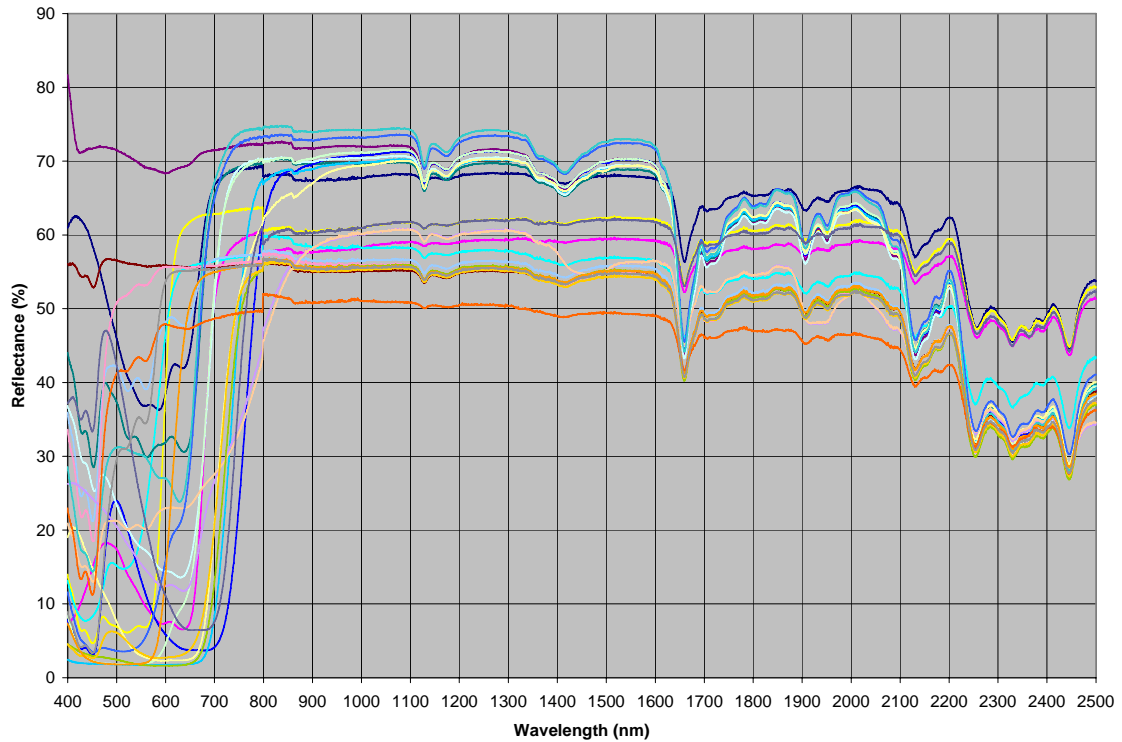
Figure 19. Reflectance spectra for solid polyester samples

This observation was explored further by calculating measures of central tendency for both the full sample set and the solid sample only subset. These results are presented graphically in Figure 20 where the bars on the left side of the chart show the mean reflectance values and the bars on the right side of the chart show the standard deviation of the reflectance values. The statistics in this chart were calculated over the two imaging bands of interest: from 400 nm to 700 nm for the visible band and from 900 nm to 1700 nm for the SWIR band. From this chart, one can see that the standard deviation of the reflectance values is always lower in the SWIR region than in the visible region. The standard deviation for the solid sample subset is substantially less than the standard deviation for the entire cohort in the SWIR region but actually increases slightly in the visible region. In addition, the mean reflectance values for both cotton and polyester were higher in the solid sample subset than for the overall sample set. The average reflectance in the SWIR region was significantly higher than the average reflectance in the visible region in all of the cases.
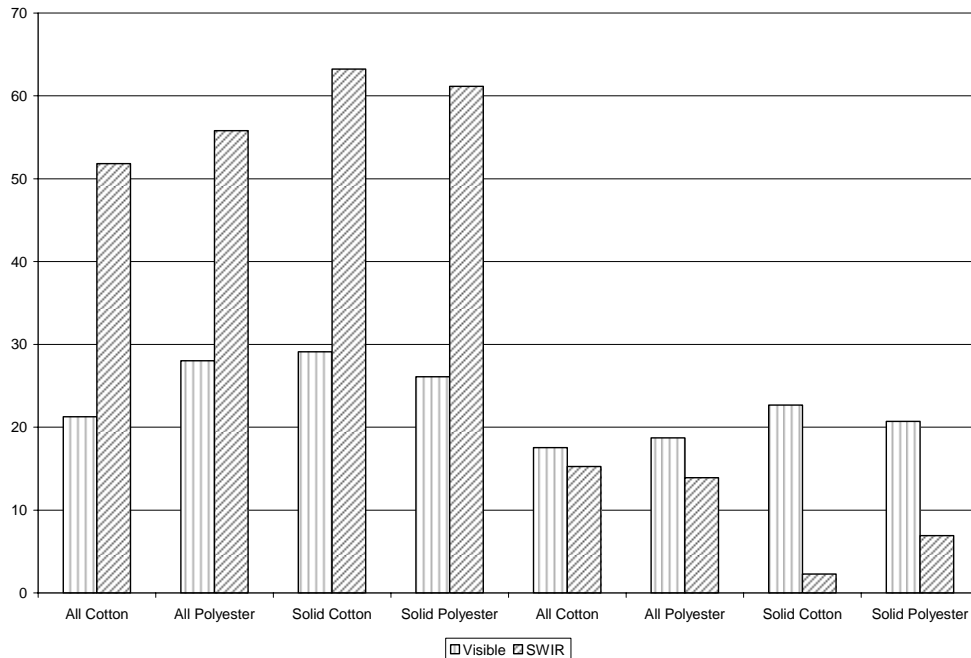
Figure 20. Mean (left side) and standard deviation (right side) of in-band reflectance values

These results confirmed the earlier hypothesis that the lower SWIR reflectance values seen in several samples were due to the graphic designs on the sample which were associated with a lower density fiber packing. This type of construction results in small openings in the sample that enable transmission of light through the sample, which leads to a lower reflectance measurement than for an optically thick sample of the same construction. Since the solid samples do not exhibit that behavior, the mean reflectance for those samples in the SWIR is higher than for the overall set. In order to help illustrate this effect, an image of a cotton sample under 250X magnification is shown in Figure 21.
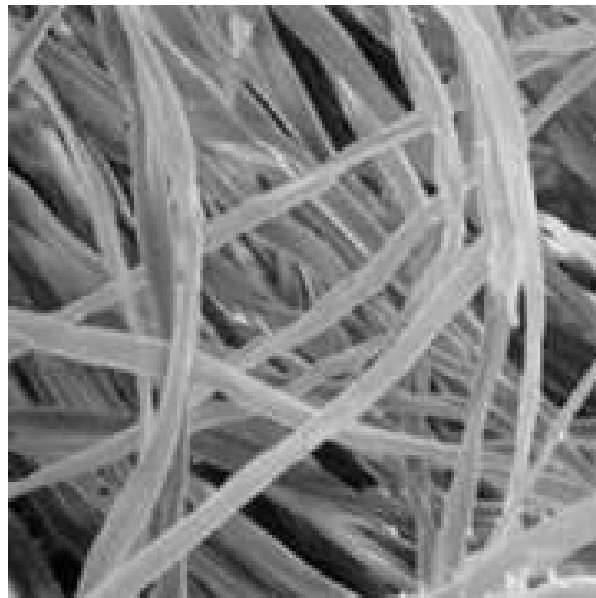
Figure 21. Microscope image of cotton fibers at 250x magnification [46]

Cotton fabrics are actually comprised of woven fibers that are on the order of 20 microns in diameter. Although the fibers are tightly packed, there are clearly gaps between them at the microscopic level. For most samples, the density of the fibers is such that it is optically thick, which leaves very few pathways through the entire sample. In the case of the fabrics with artwork, however, the periodic nature of the fiber weaves leads to relatively large gaps that are

visible even to the naked eye. These gaps allow 100% transmission and are then averaged with the reflectance values for the solid portions of the sample in the spectrometer to give an apparent diffuse reflectance measurement. The apparent reflectance measurement is dependent on the ratio of the area covered by gaps to the remaining area of the sample. Since this ratio is not constant for all sample types, there can be wide variation in the measured reflectance as seen in Figure 16 and Figure 17. The outliers for the cotton samples have SWIR reflectances as low 5% (compared to a nominal 70% reflectance for solid samples) but also appear for a number of different reflectance values. Inspection of each of these samples confirmed the presence of gaps visible to the naked eyes at varying concentrations. In order to minimize the effects described here, all subsequent analysis will be performed using only the solid sample set since the fundamental material properties are the primary interest as opposed to sample-specific behaviors.

Another interesting aspect of the data presented in Figure 20 is the relative behavior of these statistics in the visible and SWIR bands. For this sample set, the mean reflectance in the SWIR band is more than twice the mean reflectance in the visible band for both cotton and polyester. At the same time, the standard deviation of the reflectances in the SWIR band is less than half the standard deviation of the reflectances in the visible band. This quantifies the earlier observation that reflectance in the SWIR is generally higher and more spectrally uniform than in the visible band. Further analysis of this observation was performed by calculating the mean reflectance at each wavelength step over the entire measurement interval. The results of these calculations are shown graphically in Figure 22 for the full sample set and in Figure 23 for the solid sample subset. These figures show the mean and standard deviation at each wavelength for both cotton and polyester samples.
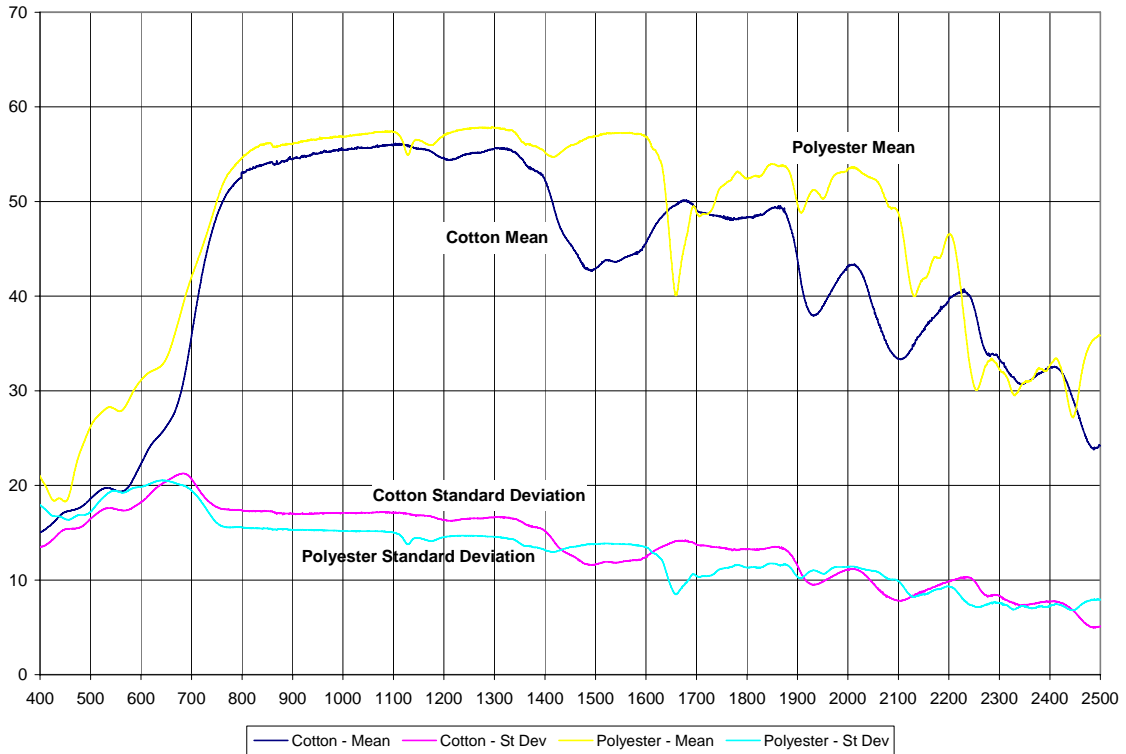
Figure 22. All sample statistics versus wavelength
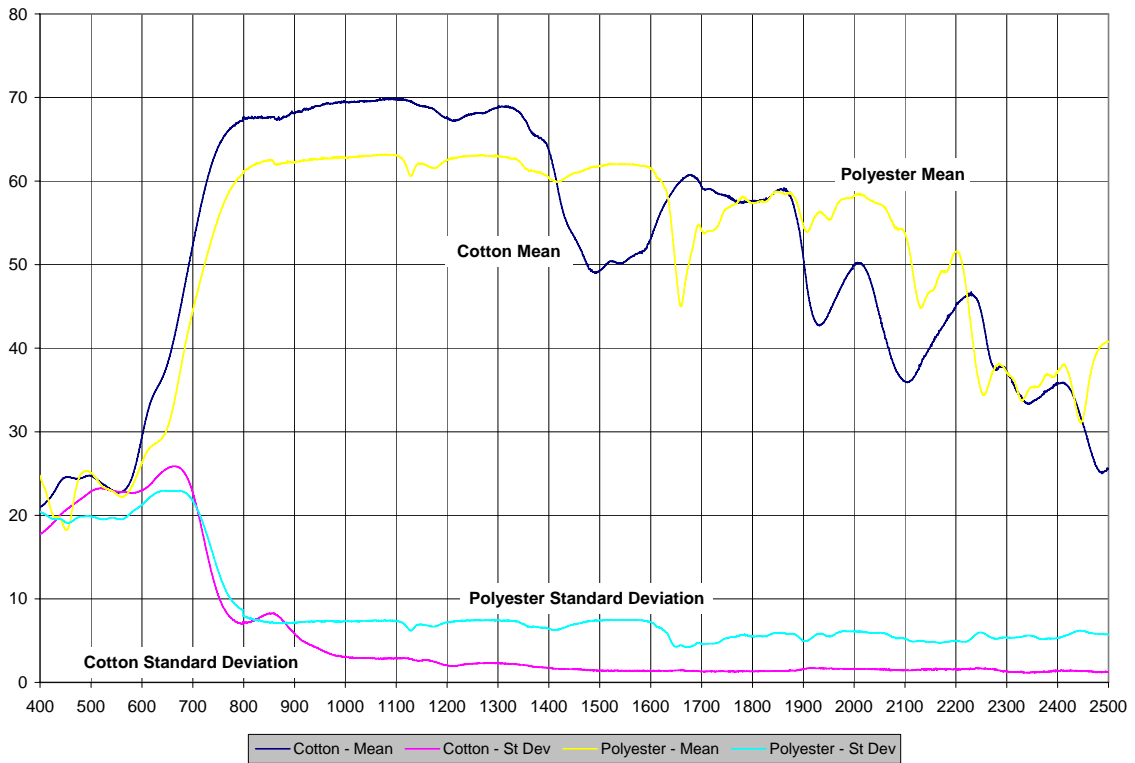
Figure 23. Solid sample statistics versus wavelength

53

In the visible portion of the measured spectra, the mean reflectance value is fairly low, around 20% and the standard deviation is approximately equal to the mean. Furthermore, the mean reflectance data exhibits a significant amount of structure in that portion of the spectrum. This can be correlated to the structure seen in the raw data presented earlier, and is most likely related to the dyes that have been added to the fabric to attain a specific visual appearance. Since the appearance of clothing is typically only of concern in the visible band, the dyes are formulated so that their color centers are located in that part of the spectrum.[47] These color centers allow the fabrics to take on the appearance of standard colors or combinations of colors as specified by the designer. There is generally no requirement for clothing dyes to have any specific characteristic in the SWIR band and, as a result, the dyes are nearly transparent in that region. In that circumstance, the reflectance of the fabric in the SWIR is characteristic of the basic material properties and is not due to the applied dye.[48]

At wavelengths just beyond those in the visible band, the mean reflectance is observed to increase substantially and rapidly, within the space of 100 nm of wavelength. Once into the SWIR region, the mean reflectance becomes extremely flat out to 1900 nm as evidenced by the sharp decrease in standard deviation throughout this region. There is structure in the SWIR region that will be compared to known molecular absorption bands. In order to illustrate this behavior, consider the behavior of sample 31163, which is a solid black cotton t-shirt knit swatch, and sample 33911, which is a solid black polyester poplin swatch. A plot of the reference spectra for these two samples, shown in Figure 24, provides a striking illustration of the behavior observed for all of the fabric samples tested. Since these samples have a black visual appearance, it is not surprising that the measured reflectance in the visual bands is fairly flat and less than 5% throughout the visible spectral region. At approximately 700 nm the

reflectance increases suddenly and at a very high rate of change to a value of approximately 70%, where it remains throughout the SWIR spectral region. Beyond the SWIR region, the reflectance develops additional structure and decreases somewhat, but not in the same manner as the initial jump in reflectance. This behavior is consistent for all of the samples tested, regardless of their color in the visual region, and demonstrates that the reflectance in the visible region is driven by the color centers of the dyes whereas the reflectance beyond the visible region is driven by the characteristics of the fabric material.
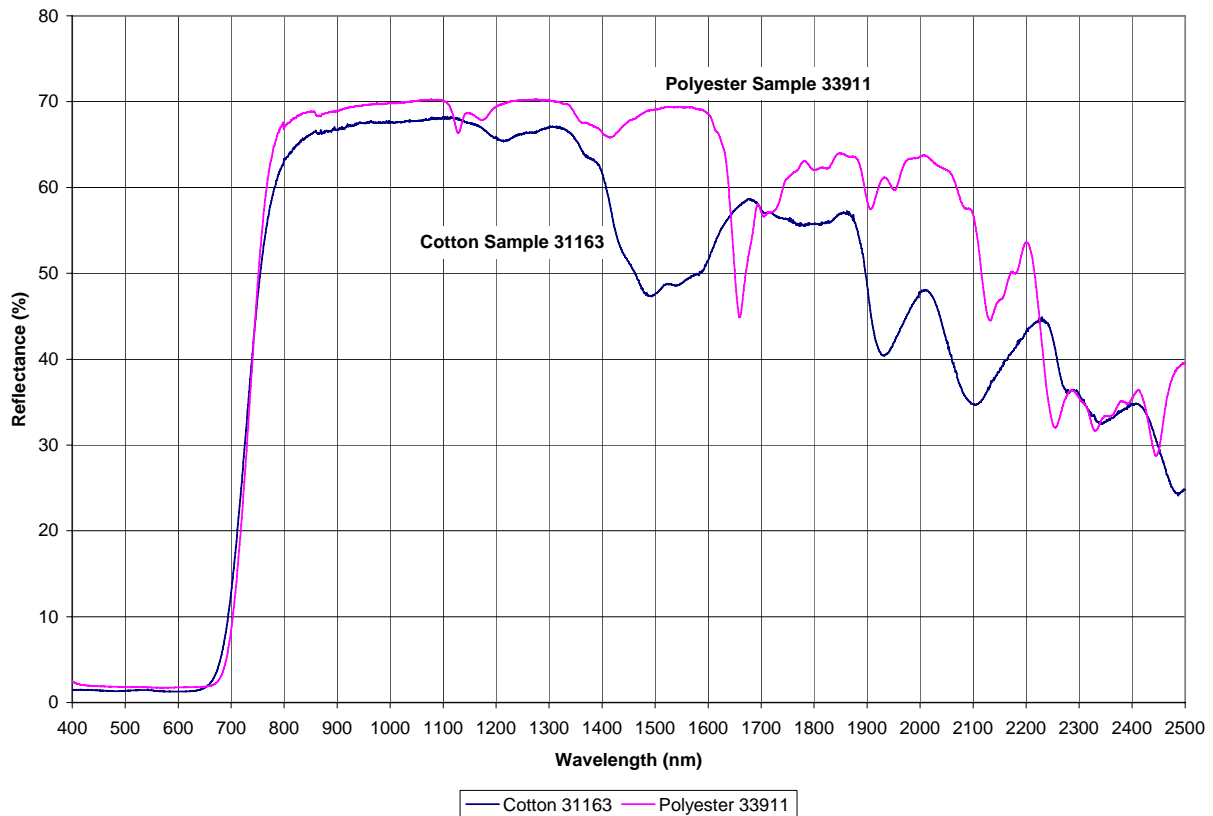

Figure 24. Reflectance spectra for black samples

In order to better understand the behavior of the cotton and polyester fibers in the SWIR region, derivative spectra were calculated in that region. The use of derivative spectra is an effective technique for sharpening features in the measured data so that they appear more

prominently in the analysis. A first derivative will also correct for any shifts in the baseline value across the spectral region, but is undesirable because the first derivative values cross zero at the wavelengths where the original data reached local maxima and exhibit peaks on the rising edge of the original data. Second derivatives address these concerns because they reach local minima at each peak in the original data, which makes it easy to identify strong absorption or reflection features. The drawback to the second derivative approach is that the spectra is significantly noisier than for a first derivative and must be smoothed mathematically to be of any practical use.[45] For reflectance spectra, standard smoothing techniques such as moving averages are not useful because they tend to destroy key features such as local maxima and minima that are needed to interpret the data. There are a number of alternative techniques that have been proposed but here a Savitzky-Golay filter was selected due to its particular suitability for smoothing spectral distributions.[49] Savitzky-Golay is a type of finite impulse response (FIR) low pass filter that behaves somewhat like a moving average but still preserves local peaks and valleys that are present in the data. This is accomplished by performing a polynomial regression on a localized window of values in the data set using a least squares approach to determine a smoothed value at each point. The degree of the polynomial used for the curve fit can be selected in the algorithm (as long as it is less than the size of the moving window) and when set to zero causes the filter to perform identically to a typical moving average. In this analysis, a cubic polynomial regression was used in the Savitzky-Golay filter implementation in MATLAB to smooth the second derivative data for the solid cotton and polyester mean reflectance spectra. The resulting data is shown in Figure 25 for the wavelength region between 800 nm and 2500 nm. Since the average reflectance spectrum was used, data in the visible

portion of the spectrum is not useful because it was influenced primarily by the dye additives and varies widely from sample to sample.
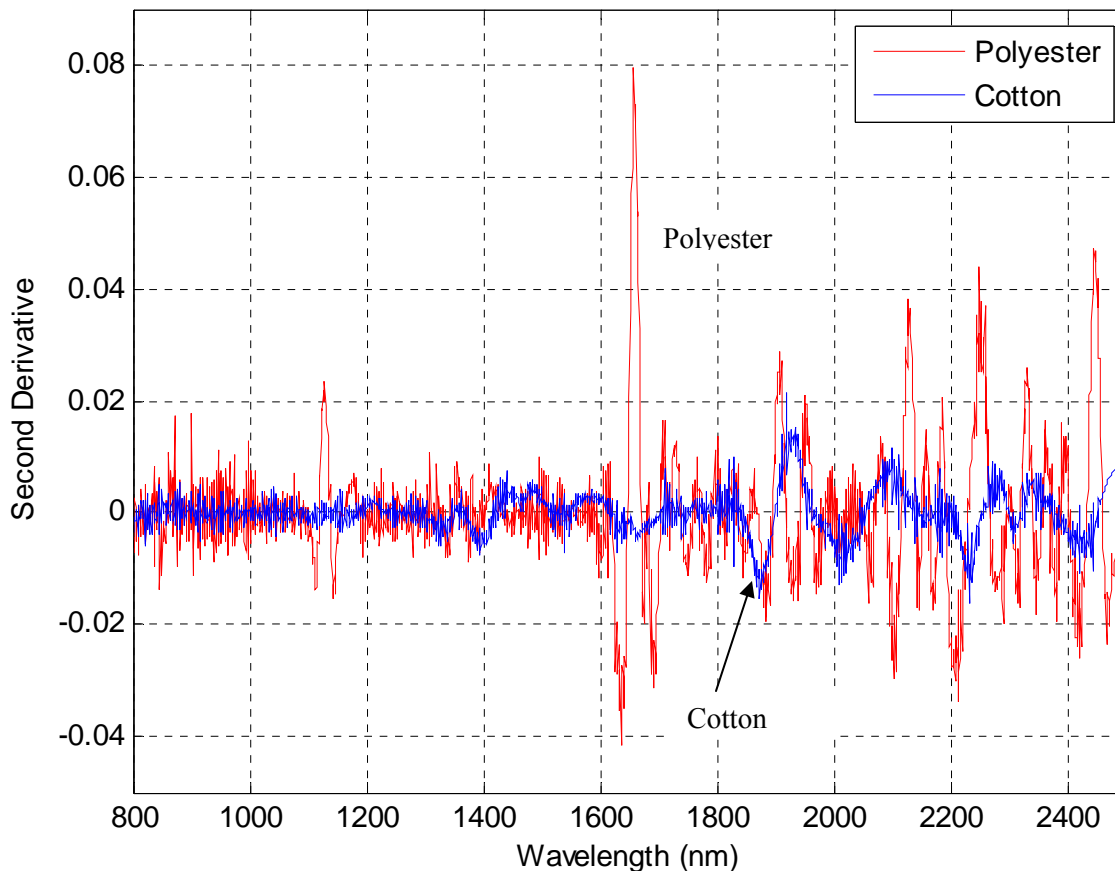
Figure 25. Derivative spectra for solid cotton and polyester samples

The derivative spectra, shown in Figure 25, make it easier to identify the absorption features for each of the textile materials tested. For instance, the strong absorption band for polyester samples that was observed at approximately 1656 nm is easily identifiable in Figure 25. From this figure, it is possible to identify seven significant absorption bands for the polyester samples and five significant absorption bands for the cotton samples. It is also immediately apparent that the absorption bands in the polyester sample are much more distinct than those in the cotton samples. The major absorption bands for cotton are centered approximately at the following wavelengths: 1196 nm, 1492 nm, 1930 nm, 2106 nm, and 2328 nm. The major

absorption bands for polyester are centered approximately at the following wavelengths: 1122 nm, 1395 nm, 1656 nm, 1900 nm, 2132 nm, 2254 nm, and 2328 nm. Although these are not the only absorption bands present in the samples, they represent the most distinct bands and were therefore considered for further analysis.

Correlating these absorption bands with physical features of the cotton and polyester samples requires consideration of molecular vibration that lead to absorption in this spectral region. A basic diatomic molecule can be modeled as a harmonic oscillator where the potential energy is described by the familiar Hooke's law in Equation 44, where k is the force constant for the bond, r is the internuclear distance at a given moment, and r_e is the nominal internuclear distance at equilibrium. [45]

$$V = \frac{1}{2}k(r-r_e)^2 \qquad\qquad\text{(Eq 44)}$$

For a harmonic oscillator, the potential energy curve is parabolic and centered about the equilibrium internuclear distance. The vibrational frequency for a harmonic oscillator is then given by the following equation:[45]

$$v = \frac{1}{2\pi}\sqrt{\frac{k}{m}} \qquad\qquad\text{(Eq 45)}$$

Where m is the reduced mass given by the following equation for the masses of the two bonded atoms:[45]

$$m = \frac{m_1 m_2}{m_1 + m_2} \qquad\qquad\text{(Eq 46)}$$

In a quantum mechanical treatment, the vibrational frequency can be used to solve the Schrödinger wave equation to provide an equation for the allowable energy levels where h is

Planck's constant and n is a vibrational quantum number that can only possess non-negative integer values:[49]

$$E_n = h\nu(n+1/2)$$
(Eq 47)

Despite this result, incident radiation can only interact with the molecule if the electric field of the incident radiation is oscillating at the same frequency as the dipole moment of the molecule. In addition, the quantum mechanical approach requires that any transition occur between adjacent energy levels such that n cannot change by more than 1 for a given transition. Since the Boltzmann distribution provides that at room temperature most molecules populate the $n = 0$ state, the fundamental absorption for the molecule occurs for transitions from $n = 0$ to $n = 1$ for an ideal harmonic oscillator. Real molecules, however, are typically anharmonic and do not behave according to these expectations. This is the case for a variety of physical reasons, particularly the presence of higher order terms in the expressions for potential energy and the dipole moment. This introduces a significant change to the potential energy function and changes its appearance from a parabolic to a curve described by the Morse function where β is a constant and D_e is the dissociation energy, which is related to the anharmonicity constant:[49]

$$V = D_e\left(1 - e^{-\beta x}\right)^2$$
(Eq 48)

One consequence of this effect is that the energy levels are not evenly spaced and are modified by an anharmonicity constant χ as shown in Equation 49 where the energy levels are expressed in terms of wavenumbers.[49]

$$G_n = \frac{E_n}{hc} = \frac{\nu}{c}\left(n + \frac{1}{2}\right) - \chi\frac{\nu}{c}\left(n + \frac{1}{2}\right)^2$$
(Eq 49)

In addition, there are no restrictions in the anharmonic case for the transition steps, so *n* can vary by more than +/- 1. Transitions of this type are referred to as overtones and have an intensity that is directly proportional to the anharmonicity constant. A variety of work has been done to calculate the wavelength associated with different bond vibrations throughout the SWIR spectral region. The measured absorption bands presented earlier were compared to the published data to identify potential matching molecules associated with each band. These results are presented in Table 8 for the cotton samples and in Table 9 for the polyester samples.[45, 48-50]

Table 8. Observed cotton absorption bands and candidate bond vibrations

Wavelength	Candidate Bond Vibration
1196 nm	C-H Second Overtone
1492 nm	N-H First Overtone
1930 nm	O-H Combination Band
2106 nm	O-H/C-O
2328 nm	C-H Combination Band

Table 9. Observed polyester absorption bands and candidate bond vibrations

Wavelength	Candidate Bond Vibration
1122 nm	CH_3 Second Overtone
1395 nm	C-H First Overtone Combination Band
1656 nm	CH_3 First Overtone
1900 nm	C=O Second Overtone
2132 nm	N-H Combination Band
2254 nm	CH_3 Combination Band
2328 nm	C-H Combination Band

The one remaining task is to consider the measured behavior for the sample set relative to the Kubelka-Munk theory that was described earlier. Recall that Kubelka and Munk described an expression for calculating the ratio of the absorption coefficient for the sample to its scattering

coefficient in terms of the measured diffuse reflectance for an optically thick sample. This relationship was given by Equation 15:

$$\frac{(1 - R_\infty)^2}{2R_\infty} = \frac{K}{S} \qquad \text{(Eq 15)}$$

Because the K-M theory assumes an optically thick material, only the solid samples described earlier were considered in this part of the analysis since the other samples did not always meet that criterion. Based on Equation 15, the mean K/S spectra were calculated for the solid cotton and polyester samples and are shown in Figure 26.
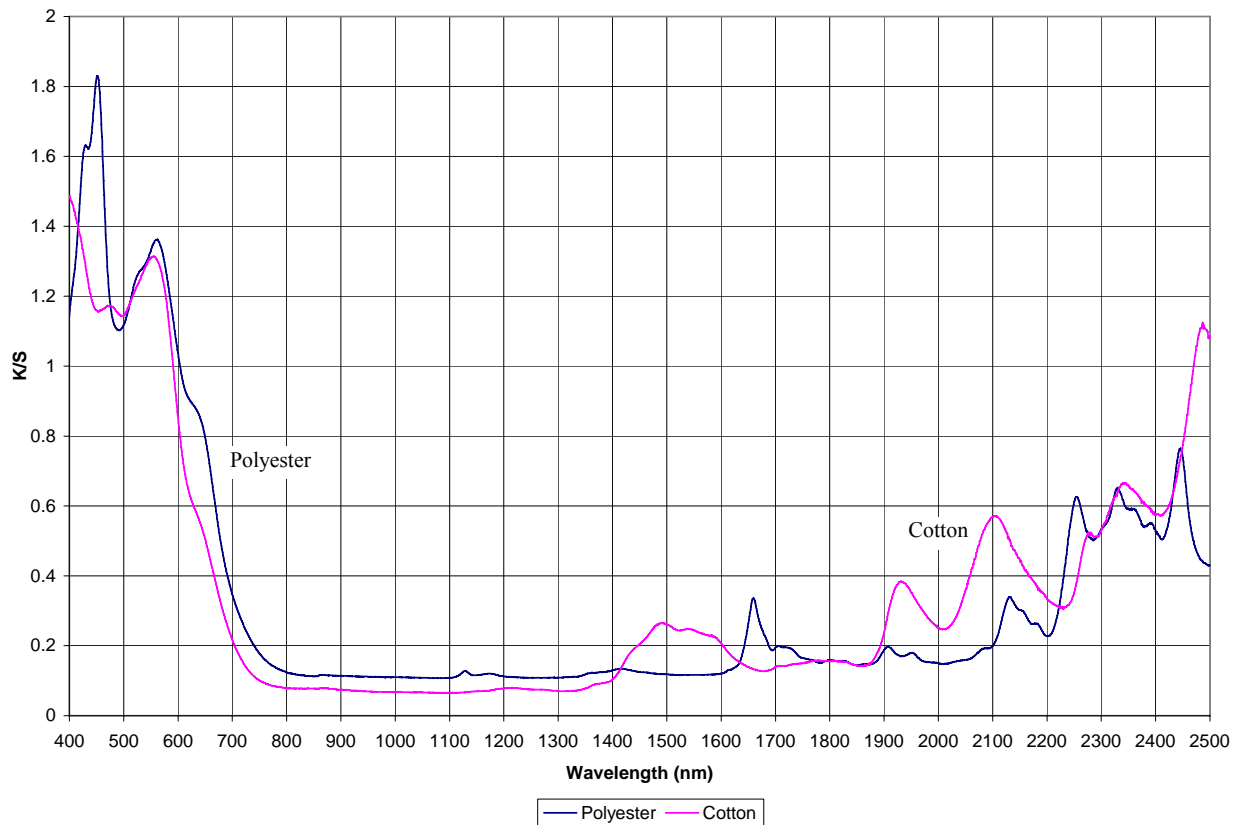
Figure 26. Mean K/S ratio for solid fabric samples

In Figure 26, larger values indicate a more strongly absorbing wavelength while lower values indicate a scattering wavelength. It is apparent from a review of this figure that samples of both

materials were strong absorbers in the visible region of the spectrum but exhibited strong scattering in the SWIR imaging band between 900 and 1700 nm. Beyond 1700 nm, spectral absorption features are plainly visible as discussed earlier, however those features are not as strong as in the visible regime. This behavior is consistent with earlier observations which noted that the color centers of the dyes added to each sample are focused in the visible region and typically exhibit very strong absorption at their design wavelengths. In addition, it explains the general tendency of clothing materials to appear highly reflective when observed by imaging systems operating in the SWIR region up to 1700 nm. This region has significant scattering effects but the few absorption bands located in the region are weak, which leads to a high diffuse reflectance value. Beyond 1700 nm, the molecular bonds in the material exhibit their characteristic absorption bands, which somewhat reduces the diffuse reflectance and adds more spectral features to its behavior. The SWIR behavior is primarily due to the fundamental material properties of cotton and polyester fibers while the visible band is primarily influenced by the dyes applied after production to give it an appearance pleasing to the human eye.

5   Conclusions/Recommendations

The diffuse reflectance of common textile materials in the short-wave infrared (SWIR) portion of the electromagnetic spectrum, defined here as wavelengths between 1.0 and 2.5 microns, has become increasingly important as that band is increasingly used for optical imaging applications in low light conditions. This increased interest is due to recent advances in detector technology, particularly Indium Gallium Arsenide (InGaAs) materials, which can be produced in large pixel formats at affordable prices and with sensitivity that is sufficient for imaging under starlight conditions.   Several phenomenological advantages in the SWIR band have also contributed, including the availability of more ambient illumination from the night sky as compared to other reflective imaging bands as well as the ability to distinguish concealed targets from the background.   The latter advantage has been observed for human targets wearing a variety of clothing types and was therefore the motivation for this work.

Cotton and polyester are two of the most common textile materials used in clothing articles today. Cotton is a naturally occurring fiber that consists primarily of cellulose and water and can be processed into an interlocked form that is optimal for creating the fine yarn needed for making cloth. This, in addition to the soft, breathable, feel has made cotton the most common textile fiber in the world today with a market share of 56% in the United States. Polyester is a synthetic fiber that is popular for clothing since it has low moisture absorption and is considered to be very durable for consumer applications. It can be woven into fibers of widely varying diameters and lengths and is therefore very versatile for textile applications. A total of 96 samples were analyzed during the experimental portion of this work, 52 of which were 100% cotton samples and 44 of which were 100% polyester swatches. Each swatch fell into one of

three general categories (art, patterned, solid) that qualitatively described its appearance. Swatches in the art category included complex, multi-color images on the sample while swatches in the patterned category included simpler recurring features such as stripes or dots. Solid swatches included a single color and had a texture that was characteristic of the component textile fabric.

The diffuse reflectance of each sample was measured in the UV, Visible, and SWIR regions using a Cary 5E spectrophotometer. The Cary 5E is a double-beam, double-grating spectrophotometer with a wavelength range of 175 nm to 3300 nm. It uses two light sources - deuterium (UV) and tungsten-halogen (VIS/SWIR) lamps – and two detectors – R928 photomultiplier tube (UV/VIS) and a cooled PbS cell (SWIR) - to cover that spectral region. A diffuse reflectance accessory (DRA) with a 110 mm diameter Polytetrafluoroethylene (PTFE) coated integrating sphere with internal PMT and PbS detectors, was used to measure the samples from 400 nm to 2500 nm in 1 nm intervals. Examination of the resulting reflectance data in the visible spectral region between 400 nm and 700 nm showed a significant amount of structure that made it difficult to ascertain any trend between the various samples or between the cotton and polyester cohorts. However, between 700 and 900 nm, the reflectance tended to increase for both sample types and then become fairly uniform throughout the SWIR imaging band (900 nm to 1700 nm, corresponding to lattice-matched InGaAs detectors) with a reflectance value in the range between 50% and 70%. In both cases, but especially in the cotton cohort, there were also several outlying samples that had significantly lower reflectance values throughout the SWIR region as compared to the mean reflectance values.

The wide variation in diffuse reflectance spectra in the visible portion of the data was found to be due to the dyes that have been added to the fabric to attain a specific visual appearance. Since the appearance of clothing is typically only of concern in the visible band, the dyes are formulated so that their color centers are located in that part of the spectrum. There is generally no requirement for clothing dyes to have any specific characteristic in the SWIR band and, as a result, the dyes are nearly transparent in that region and the diffuse reflectance is instead characteristic of the material. Despite this, some spectral structure was observed in the SWIR portion of the data, particularly at longer wavelengths. Second derivative spectra were calculated for both the cotton and polyester samples in order to better understand this behavior. These derivative spectra helped identify a number of absorption bands that were characteristic of each respective material. The bands were then compared to known molecular absorption bands to identify the corresponding molecules associated with each band.

Finally, the behavior of the samples was considered in terms of the Kubelka-Munk theory presented earlier. These calculations demonstrated that both materials were strong absorbers in the visible region of the spectrum but exhibited significant scattering in the SWIR imaging band between 900 and 1700 nm. Beyond 1700 nm, spectral absorption features were evident but were not as strong as in the visible regime. This behavior was consistent with the earlier conclusion that the color centers of the dyes added to each sample are focused in the visible region and typically exhibit very strong absorption only at their design wavelengths. In addition, it explained the general tendency of clothing materials to appear highly reflective when observed by imaging systems operating in the SWIR region up to 1700 nm. This region has significant scattering effects but the few absorption bands located in the region are weak, which leads to a high diffuse reflectance that is independent of the dyes added to the fabric. As a result, fabrics

appear to be uniform and highly reflective in the SWIR band regardless of their appearance in the visible spectral region.

This thesis has identified a set of unique spectral fingerprints in the SWIR region that allows one to distinguish between cotton and polyester fibers. These fingerprints can be obtained simply by measuring the diffuse reflectance spectra (or alternatively the absorptance spectra) of a particular sample in the SWIR regime using a spectrophotometer. Most importantly, these fingerprints can be used to distinguish between cotton and polyester regardless of their visible color and/or texture, which provides a significant advantage given the wide variety of fabrics that are produced today. This capability has applications in a number of areas, including low light level imaging and target recognition as well as quality testing for materials during textile production.

Future work should expand these investigations to other materials that are commonly used in clothing such as wool or nylon. An important aspect is to consider blends of fabrics since many clothing articles today use these combinations to achieve a particular look or feel. While the dyes used in the test samples in this work are characteristic of those used in clothing material, one must also investigate whether other dyes exist that exhibit spectral behavior in the SWIR region or whether such dyes could be designed if they are not already in use. Investigation in all of these areas is needed to fully understand the diffuse reflectance behavior of fabrics in the SWIR spectral region.

6 References

1. Hansen, M.P. and D.S. Malchow. *Overview of SWIR detectors, cameras, and applications*. 2008. Orlando, FL, USA: SPIE - The International Society for Optical Engineering.
2. Richmond, R., R. Stettner, and J. Glessner. *Eye safe laser radar focal plane array for three-dimensional imaging*. 2000. Orlando, FL, USA: Society of Photo-Optical Instrumentation Engineers, Bellingham, WA, USA.
3. Ettenberg, M.H., et al. *High-resolution SWIR arrays for imaging at night*. 2004. Orlando, FL, USA: SPIE-Int. Soc. Opt. Eng.
4. D'Souza, A.I., et al. *SWIR to LWIR HDVIP HgCdTe detector array performance*. 2006. Orlando, FL, USA: SPIE - The International Society for Optical Engineering.
5. Beck, J., et al., *The HgCdTe electron avalanche photodiode.* Journal of Electronic Materials, 2006. **35**(6): p. 1166-73.
6. Boisvert, J., et al. *Characterization of InGaAsP/InP APD arrays for SWIR imaging applications*. 2006. Orlando, FL, USA: SPIE - The International Society for Optical Engineering.
7. Destefanis, G. and P. Tribolet. *Advanced MCT technologies in France*. 2007. Orlando, FL, United States: SPIE, Bellingham WA, WA 98227-0010, United States.
8. Beystrum, T., et al. *Low cost PbSalt FPA's*. 2004. Orlando, FL, United States: International Society for Optical Engineering, Bellingham, WA 98227-0010, United States.
9. Rhiger, D.R., et al. *Progress with type-II superlattice IR detector arrays*. 2007. Orlando, FL, United States: SPIE, Bellingham WA, WA 98227-0010, United States.
10. Schowengerdt, R.A., *Remote Sensing.* Civil & Environmental. 2007: Academic Press. 1.
11. Aube, M., et al. *Light pollution modelling and detection in a heterogeneous environment: Toward a night time Aerosol optical Depth retrieval method*. 2005. San Diego, CA, United States: International Society for Optical Engineering, Bellingham WA, WA 98227-0010, United States.
12. Favero, G., et al., *Measurements of light pollution of Padua.* Memorie della Societa Astronomica Italiana, 2000. **71**(1): p. 223-30.
13. Pedani, M., *Light pollution at the Roque de los Muchachos Observatory.* New Astronomy, 2004. **9**(8): p. 641-650.
14. Webster, T., *Light Pollution and Astronomy - Are We Still Relevant?* Lighting Journal (Rugby, England), 2004. **69**(1): p. 56.
15. Leinert, C., et al., *The 1997 reference of diffuse night sky brightness.* Astronomy & Astrophysics Supplement Series, 1998. **127**(1): p. 1-99.
16. R. Sloan, J.H.S., D. Williams, *Thermal Radiation from the Atmosphere.* Journal of the Optical Society of America, July 1956. **46**(1): p. 543-547.
17. Wallace, L., *The OH Nightglow Emission.* Journal of the Atmospheric Sciences, January 1962. **19**(1): p. 1-16.
18. Vatsia, M., *Atmospheric Optical Environment*. 1972, Research and Development Technical Report ECOM-7023.
19. Lane, R.N. *The SWIR advantage*. 1995. San Diego, CA, USA: Society of Photo-Optical Instrumentation Engineers, Bellingham, WA, USA.

20. Norton, M.C., R. Kindsfather, and R. Dixon. *Shortwave (1 to 2.8 um) imagery applications for fun and profit*. in *Terrorism and Counter-Terrorism Methods and Technologies*. 1997. Boston, MA, USA: SPIE.

21. Haran, T.L., J.C. James, and G. Bennett, *Comparison of Spectral Imaging Band Performance at Night*. 2007, Georgia Institute of Technology: Atlanta, GA.

22. Gustav Mie, *Beiträge zur Optik trüber Medien, speziell kolloidaler Metallösungen*. Annalen der Physik, 1908. **330**(3): p. 377-445.

23. Silvy, J., *Contribution to the study of multiple scattering of light within the scope of the scattering approximation*. Revue d'Optique (Theorique et Instrumentale), 1961. **40**(10): p. 495-517.

24. Kubelka, P. and F. Munk, *Reflection characteristics of paints*. Zeitschrift fur Technische Physik, 1931. **12**: p. 593-601.

25. Schuster, A., *Radiation through a foggy atmosphere*. Astrophysical Journal, 1905. **21**: p. 1-22.

26. Kubelka, P., *New contributions to the optics of intensely light-scattering materials. I*. Journal of the Optical Society of America, 1948. **38**: p. 448-457.

27. Christy, A.A., et al., *Effect of particle size on diffuse reflectance infrared spectra of polystyrene spheres*. Vibrational Spectroscopy, 1993. **5**(2): p. 233-244.

28. Philips-Invernizzi, B., D. Dupont, and C. Caze, *Bibliographical review for reflectance of diffusing media*. Optical Engineering, 2001. **40**(6): p. 1082-92.

29. Chandrasekhar, S., *Radiative Transfer*. 1960, New York: Courier Dover Publications.

30. Mudgett, P.S. and L.W. Richards, *Multiple scattering calculations for technology*. Applied Optics, 1971. **10**(7): p. 1485-502.

31. Pierce, P.E. and R.T. Marcus, *Radiative Transfer Theory Solid Color-Matching Calculations*. Color Research and Application, 1997. **22**(2): p. 72-87.

32. Hulst, H.C.v.d., *Multiple Light Scattering, Tables, Formulas, and Applications*. Vol. 1 and 2. 1980, New York: Academic Press.

33. Shu, F.H., *The Physics of Astrophysics*. Vol. 1. 1991, Mill Valley, CA: University Science Books.

34. Allen, E., *PREDICTION OF OPTICAL PROPERTIES OF PAINTS FROM THEORY (WITH SPECIAL REFERENCE TO MICROVOID PAINTS)*. Journal of Paint Technology, 1973. **45**(584): p. 65-72.

35. Kourganoff, V., *On a generalization of the variational method for problems of radiative transfer*. Astrophysical Journal, 1950. **111**: p. 443-445.

36. Ross, W.D., *Theoretical computation of light scattering power. Comparison between TiO//2 and air bubbles*. 1971. **43**(563): p. 50-66.

37. Giovanelli, R.G., *Reflection by semi-infinite diffusers*. Optica Acta, 1955. **2**(4): p. 153-162.

38. Prahl, S. *Optical Absorption of Water*. [cited 2008 August 10, 2008]; Available from: http://omlc.ogi.edu/spectra/water/index.html.

39. Chaplin, M. *Water Structure and Science*. August 10, 2008]; Available from: http://www.lsbu.ac.uk/water/vibrat.html.

40. Leong, H.C., *Imaging and Reflectance Spectroscopy for the Evaluation of Effective Camouflage in the SWIR*, in *Department of Physics*. 2007, Naval Postgraduate School: Monterey, CA.

41. *Cotton for Nonwovens: A Technical Guide*. August 10, 2008]; Available from: http://www.cottoninc.com/Nonwovens/CottonNonwovens/.

42. Brandrup, J., E.H. Immergut, and E.A. Grulke, *Polymer Handbook*. 4th ed. 1999, New York: Wiley.

43. Cook, J.G., *Handbook of Textile Fibers*. 5th ed. 1984, Durham, England: Merrow.

44. Hutten, I.M., *Handbook of Nonwoven Filter Media*. 1st ed. 2007, Burlington, MA: Butterworth-Heinemann.

45. Burns, D.A. and E.W. Ciurczak, *Handbook of Near-Infrared Analysis*. 3rd ed. Practical Spectroscopy. 2008, Boca Raton: CRC Press. 808.

46. Broadbent, A.D. and F. Motamedian. *Modeling light reflection from colored filament assemblies*. 2000. San Diego, CA, USA: Society of Photo-Optical Instrumentation Engineers, Bellingham, WA, USA.

47. El Sherif, M., O.A. Bayoumi, and T.Z.N. Sokkar, *Prediction of absorbance from reflectance for an absorbing-scattering fabric*. Color Research and Application, 1997. **22**(1): p. 32.

48. Papini, M., *Study of the radiative properties of natural and synthetic fibers in the 0.25-2.5 μm region*. Applied Spectroscopy, 1989. **43**(8): p. 1475-1481.

49. Siesler, H.W., *Near-Infrared Spectroscopy: Principles, Instruments, and Applications*. 2002, Weinheim: Wiley-VCH.

50. Marcelo Blanco, J.C., Hortensia Iturriaga, Santiago Maspoch, Enriqueta Bertran, *Analysis of Cotton-Polyester Yarns by Near-Infrared Reflectance Spectroscopy*. Analyst, 1994. **119**.

Appendix: Test Articles

Code	Name	Color	Type	Material
20698	Tahitian Sunset Swatch	Black	Art	Cotton
20699	Wailea Coast Sun Swatch	Ebony	Art	Cotton
20771	Orchid Cove Sun N Shade Swatch	Black	Art	Cotton
25929	African Print Swatch	Multi animal print	Art	Cotton
26491	African Print Swatch	Blue Orange Black Whi	Art	Cotton
27401	Western Style Swatch	Multi-colored on Red	Art	Cotton
27735	African Print Swatch	Burg, green blue blac	Art	Cotton
27885	Colorful Sneakers Swatch	Multi-colored on Turq	Art	Cotton
27888	Sassy Sealife Swatch	Blue and Orange on Gr	Art	Cotton
27896	Hawaiian Print Swatch	Yellow Orange Green R	Art	Cotton
29852	Rocket Ships Swatch	Multi Brights on Blac	Art	Cotton
32787	Dolphins Swatch	Shades of Blue	Art	Cotton
34181	African Animals Swatch	Multi	Art	Cotton
34580	Cotton Flannel Print Swatch	Multi on Blue	Art	Cotton
34851	Patriotic Print Swatch	Red/White/Blue/Black	Art	Cotton
34869	Hawaiian Print Swatch	Multi	Art	Cotton
35634	All Sports Swatch	Multi on Navy	Art	Cotton
35979	Color Quake Swatch	Multi on Shades of Pu	Art	Cotton
35988	Hawaiian Sunset Swatch	Multi	Art	Cotton
35989	American Heritage Swatch	Multi	Art	Cotton
36267	Lahaina Swatch	Black	Art	Cotton
36476	Hawaiian Print Swatch	Multi on Green	Art	Cotton
36477	Hawaiian Print Swatch	Multi on Red	Art	Cotton
36495	Ropin Swatch	Multi on Tan	Art	Cotton
36832	Surboard Collection Swatch	Multi on Pink	Art	Cotton
26460	African Print Swatch	Red, Green, Black,Yel	Patterned	Cotton
26474	African Print Swatch	Yellow Green Black Or	Patterned	Cotton
26690	Cotton Polka Dots Swatch	Black with White dots	Patterned	Cotton
26696	Cotton Polka Dots Swatch	Multi-colored on Blac	Patterned	Cotton
26729	Cotton Polka Dots Swatch	Royal Blue/White	Patterned	Cotton
26754	Cotton Polka Dots Swatch	Blue Red Yellow White	Patterned	Cotton
31809	Seersucker Shirting Swatch	Pink, Green, Yellow	Patterned	Cotton
34668	Camouflage Twill Swatch	Brown/Tan/Khaki	Patterned	Cotton
34671	Camouflage Print Swatch	Digital	Patterned	Cotton
34856	Patriotic Print Swatch	Red/White	Patterned	Cotton
35197	Seersucker Shirting Swatch	Turquoise/Navy Check	Patterned	Cotton
35645	Cotton Flannel Print Swatch	Multi	Patterned	Cotton
35811	African Print Swatch	Green/Red/Black/Purpl	Patterned	Cotton
36364	Seersucker Shirting Swatch	Pink/Purple Plaid	Patterned	Cotton

37368	Retro Dots Swatch	Blue/Lime/Ivory	Patterned	Cotton
37665	Camouflage Print Swatch	Blues	Patterned	Cotton
29982	Cotton T-Shirt Knit Swatch	Prism Violet	Solid	Cotton
29995	Cotton T-Shirt Knit Swatch	chintz rose	Solid	Cotton
29999	Cotton T-Shirt Knit Swatch	Blue Bell	Solid	Cotton
30004	Cotton T-Shirt Knit Swatch	Chili Pepper	Solid	Cotton
30008	Cotton T-Shirt Knit Swatch	Pastel Blue	Solid	Cotton
30009	Cotton T-Shirt Knit Swatch	Sunkist Coral	Solid	Cotton
30013	Cotton T-Shirt Knit Swatch	Pale Banana	Solid	Cotton
31163	Cotton T-Shirt Knit Swatch	Black	Solid	Cotton
36411	Cotton Interlock Swatch	Lime	Solid	Cotton
36412	Cotton Interlock Swatch	Stop Sign	Solid	Cotton
36413	Cotton Interlock Swatch	Royal Blue	Solid	Cotton
20764	Tangier Sun N Shade Swatch	Sage	Art	Polyester
28276	Seaside Lily Sun N Shade by Wa	Key Lime	Art	Polyester
28277	Isla Bonita Sun N Shade by Wav	Ocean	Art	Polyester
28278	Wailea Coast Sun N Shade by Wa	Flax	Art	Polyester
28282	Essence Sun N' Shade by Waver1	Onyx	Art	Polyester
33785	Sadie Swatch	Azalea	Art	Polyester
33787	Whim Swatch	Mist	Art	Polyester
33788	Curvature Swatch	Foliage	Art	Polyester
33793	Fiji Swatch	Midnight	Art	Polyester
33796	Jefferson Swatch	Café	Art	Polyester
20766	Biscayne Bay Sun N Shade Swatch	Dune	Patterned	Polyester
20769	Rodeo Drive Sun N Shade Swatch	Sea Spray	Patterned	Polyester
20770	Beach Umbrella Sun N Shade Swatch	Pink/Black	Patterned	Polyester
20772	Marina Del Ray Sun N Shade Swatch	Surf	Patterned	Polyester
28279	Beach Umbrella Sun N Shade by Waver1	Flax	Patterned	Polyester
33794	Bistro Stripe Swatch	Midnight	Patterned	Polyester
33799	Larrabee Swatch	Mocha	Patterned	Polyester
36268	La Jolla Stripe Swatch	Aqua	Patterned	Polyester
28280	Sunburst Sun N Shade by Waver1	Chocolate	Solid	Polyester
31039	Polyester Shantique Swatch	Lilac	Solid	Polyester
31498	Polyester Charmeuse Swatch	Ocean	Solid	Polyester

32750	Polyester Charmeuse Swatch	Poppy	Solid	Polyester
33512	Polyester Charmeuse Swatch	Canteloupe	Solid	Polyester
33907	Polyester Poplin Swatch	White	Solid	Polyester
33908	Polyester Poplin Swatch	Ivory	Solid	Polyester
33909	Polyester Poplin Swatch	Gray	Solid	Polyester
33910	Polyester Poplin Swatch	Green	Solid	Polyester
33911	Polyester Poplin Swatch	Black	Solid	Polyester
33912	Polyester Poplin Swatch	Copen	Solid	Polyester
33913	Polyester Poplin Swatch	Burgundy	Solid	Polyester
33914	Polyester Poplin Swatch	Royal Blue	Solid	Polyester
34661	Polyester Poplin Swatch	Champagne	Solid	Polyester
34662	Polyester Poplin Swatch	Banana	Solid	Polyester
34705	Sunburst Sun N Shade Swatch	Keylime	Solid	Polyester
35203	Polyester Poplin Swatch	Light Blue/Navy Cross	Solid	Polyester
35204	Polyester Poplin Swatch	Tan/Brown Crossdye	Solid	Polyester
36277	FR Poplin Swatch	Chili	Solid	Polyester
36282	FR Poplin Swatch	Pistachio	Solid	Polyester
36342	Polyester Poplin Swatch	Navy	Solid	Polyester
36343	Polyester Poplin Swatch	Hunter	Solid	Polyester
36344	Polyester Poplin Swatch	Red	Solid	Polyester
37140	Polyester Charmeuse Swatch	Sunshine Yellow	Solid	Polyester
37141	Polyester Charmeuse Swatch	Cyan	Solid	Polyester
37701	Polyester Poplin Swatch	Mango	Solid	Polyester